J. Fluid Mech. (2010), *vol.* 660, *pp.* 282–315.
doi:10.1017/S0022112010002752

Investigation of the subgrid-scale fluxes and their production rates in a convective atmospheric surface layer using measurement data

QINGLIN CHEN, SHUAISHUAI LIU AND CHENNING TONG†

Department of Mechanical Engineering, Clemson University, Clemson, SC 29634, USA

(Received 2 June 2009; revised 10 May 2010; accepted 10 May 2010; first published online 19 July 2010)

The subgrid-scale (SGS) potential temperature flux and stress in the atmospheric surface layer are studied using field measurement data. We analyse the mean values of the SGS temperature flux, the SGS temperature flux production rate, the SGS temperature variance production rate, the SGS stress and the SGS stress production rate conditional on both the resolvable-scale velocity and temperature, which must be reproduced by SGS models for large-eddy simulation to reproduce the one-point resolvable-scale velocity–temperature joint probability density function (JPDF). The results show that the conditional statistics generally depend on the resolvable-scale velocity and temperature fluctuations, indicating that these conditional variables have strong influences on the resolvable-scale statistics. The dependencies of the conditional SGS stress and the SGS stress production rate, which are partly due to the effects of flow history and buoyancy, suggest that model predictions of the SGS stress also affect the resolvable-scale temperature statistics. The results for the conditional flux and the conditional flux production rate vectors have similar trends. These conditional vectors are also well aligned. The positive temperature fluctuations associated with updrafts are found to have a qualitatively different influence on the conditional statistics than the negative temperature fluctuations associated with downdrafts. The conditional temperature flux and the temperature flux production rate predicted using several SGS models are compared with measurements in statistical *a priori* tests. The predictions using the nonlinear model are found to be closely related to the predictions using the Smagorinsky model. Several potential effects of the SGS model deficiencies on the resolvable-scale statistics, such as the overprediction of the vertical mean temperature gradient and the underprediction of the vertical temperature flux, are identified. The results suggest that efforts to improve the LES prediction of a resolvable-scale statistic must consider all the relevant SGS components identified using the JPDF equation and the surface layer dynamics. This study also provides impetus for further investigations of the JPDF equation, especially analytical studies on the relationship between the JPDF and the SGS terms that govern its evolution.

Key words: turbulent boundary layers, turbulence modelling, turbulence simulation

† Email address for correspondence: ctong@ces.clemson.edu

1. Introduction

Large-eddy simulation (LES) is an important approach for simulating turbulent flows. When the filter scale is in the inertial range, the energy-containing scales are well resolved and most of the turbulent stress and fluxes are contained in the resolvable scales (Lilly 1967; Domaradzki, Liu & Brachet 1993; Borue & Orszag 1998). LES results with such filter scales are generally insensitive to the subgrid-scale (SGS) model employed (Nieuwstadt & de Valk 1987; Mason 1994).

In LES of high-Reynolds-number turbulent boundary layers, however, the filter scale in the near-wall region is inevitably in the energy-containing scale range (Kaimal *et al.* 1972; Mason 1994; Peltier *et al.* 1996; Tong *et al.* 1998; Tong, Wyngaard & Brasseur 1999). As a result, significant amounts of the turbulent stress and fluxes are carried by the SGS model, resulting in strong dependence of the near-wall results on the SGS model (e.g. Mason & Thomson 1992; Tong *et al.* 1999). Consequently, any deficiencies of SGS models are likely to result in inaccuracies in the LES statistics in the near-wall region. For example, the standard Smagorinsky model overpredicts the mean temperature gradient and the mean temperature variance, but underpredicts the mean vertical temperature flux in the LES of the unstable atmospheric boundary layer (ABL) (Mason & Thomson 1992; Sullivan, McWilliams & Moeng 1994). An important question in improving SGS models, therefore, is how the SGS turbulence and SGS models affect the resolvable-scale statistics under these conditions.

Previous studies of SGS physics typically have focused on the energy transfer rate from the resolvable to the subgrid scales (e.g. Domaradzki *et al.* 1993; Borue & Orszag 1998). A limitation of such studies is that they do not provide information on how the SGS turbulence affects the resolvable-scale statistics. Previous SGS model tests generally compared the instantaneous modelled SGS stress and fluxes with measurements or direct numerical simulation (DNS), i.e. *a priori* tests, or compared the LES statistics with those obtained using measurements or DNS, i.e. *a posteriori* tests (e.g. Clark, Ferziger & Reynolds 1979; McMillan & Ferziger 1979; Bardina, Ferziger & Reynolds 1980; Nieuwstadt & de Valk 1987; Piomelli, Moin & Ferziger 1988; Lund & Novikov 1992; Mason & Thomson 1992; Domaradzki *et al.* 1993; Piomelli 1993; Härtel *et al.* 1994; Liu, Meneveau & Katz 1994; Mason 1994; Meneveau 1994; Peltier *et al.* 1996; Juneja & Brasseur 1999; Sarghini, Piomelli & Balaras 1999; Tao, Katz & Meneveau 2000; Porté-Agel *et al.* 2001; Sullivan *et al.* 2003). A major limitation of such tests is their lack of ability to relate SGS model to the resolvable-scale statistics. For *a priori* tests, it is difficult to predict the effects of SGS model performance on LES results, while for *a posteriori* tests, it is difficult to relate the deficiencies of LES results to specific model behaviours (Chen & Tong 2006).

To overcome these limitations, we developed a systematic approach (Chen *et al.* 2003, 2005; Chen & Tong 2006; Chen *et al.* 2009) to understand the effects of SGS turbulence on the resolvable-scale statistics and those of SGS models on LES statistics. The approach is based on the transport equations of the resolvable-scale velocity joint probability density function (JPDF) and the velocity–temperature JPDF. It analyses the SGS terms that govern the evolution of the JPDFs, which are conditional statistics containing SGS stress and fluxes (see (1.5) and (1.6)). The conditional statistics obtained from measurements are analysed to study the effects of SGS turbulence on the resolvable-scale statistics. In our new *a priori* tests, the conditional statistics obtained using SGS models are compared with those obtained from measurements (Chen & Tong 2006). In the new *a posteriori* tests, the conditional statistics obtained from LES are compared with those obtained from measurements (Chen *et al.* 2009).

This approach has several advantages over the traditional SGS model test methods. First, it deals with the resolvable-scale statistics, of which accurate predictions are the primary objective of LES. By contrast, traditional methods often compare instantaneous SGS variables. Consequently, the results are very difficult to interpret. Second, unlike the filtered Navier–Stokes equations and the scalar transport equation, the JPDF transport equation does not produce chaotic solutions. In addition, previous analytical results of similar equations (Jaberi, Miller & Givi 1996; Sabelnikov 1998) can be used to understand the behaviour of SGS turbulence and SGS models (Chen & Tong 2006; Chen *et al.* 2009). Third, the JPDF equations can be used to study the SGS turbulence and to perform both statistical *a priori* and *a posteriori* tests of SGS models, allowing direct comparisons of the two types of test results, whereas the traditional *a priori* and *a posteriori* tests deal with instantaneous SGS variables and LES statistics, respectively; therefore, their results cannot be compared directly. Chen & Tong (2006) and Chen *et al.* (2009) emphasized that the new *a priori* tests provide a strong connection between the modelled SGS terms and the resolvable-scale velocity JPDF; therefore, they are qualitatively different from the traditional *a priori* tests based on correlations of the measured and modelled SGS variables.

Chen & Tong (2006) used this approach to study the SGS turbulence in the surface layer of the ABL and performed *a priori* tests of several SGS models. They identified several deficiencies of the SGS models that affect the LES statistics. They argued that the overpredictions of the mean shear and streamwise velocity variance near the surface by the Smagorinsky model are partly due to the underprediction of the anisotropy of the SGS stress and its variations in the near-wall region. They also pointed out that the underprediction of the vertical velocity skewness is likely due to the inability of the Smagorinsky model to predict the asymmetry in the production rate of the vertical normal component of the SGS stress. These analyses based on the JPDF equation provide important knowledge for improving SGS models. Using LES fields and measurement data, Chen *et al.* (2009) performed *a posteriori* tests based on the JPDF equation. The same model strengths and deficiencies were observed. The consistency between the *a priori* and *a posteriori* tests suggests that there is a close relationship between these tests. Unlike the traditional tests, the new *a priori* tests are capable of predicting the *a posteriori* model performance.

The present work studies the influence of the SGS temperature flux and the SGS stress on the resolvable-scale velocity–temperature JPDF in the horizontally homogeneous ABL by analysing the JPDF transport equation, which can be derived following the method given by Pope (1985). Differentiating the JPDF,

$$f = \left\langle \delta[\theta^r - \psi] \prod_{i=1}^{3} \delta\left[u_i^r - v_i\right] \right\rangle, \tag{1.1}$$

with respect to time, we obtain

$$\frac{\partial f}{\partial t} = -\frac{\partial}{\partial v_i}\left\{ \left\langle \frac{\partial u_i^r}{\partial t} | \boldsymbol{u}^r = \boldsymbol{v}, \theta^r = \psi \right\rangle f \right\} - \frac{\partial}{\partial \psi}\left\{ \left\langle \frac{\partial \theta^r}{\partial t} | \boldsymbol{u}^r = \boldsymbol{v}, \theta^r = \psi \right\rangle f \right\}, \tag{1.2}$$

where δ is the Dirac delta function, and $\boldsymbol{v}$ and ψ are the sample-space variables for the resolvable-scale velocity $\boldsymbol{u}^r$ and the resolvable-scale fluctuating potential temperature θ^r (the superscript r denotes a resolvable-scale variable), respectively, and the angle brackets denote an ensemble mean. Substituting the time derivatives, $\partial u_i^r/\partial t$ and $\partial \theta^r/\partial t$, in (1.2) with the right-hand side of the equation for the resolvable-scale

velocity:

$$\frac{\partial u_i^r}{\partial t} = -\frac{\partial u_j^r u_i^r}{\partial x_j} - \frac{\partial \tau_{ij}}{\partial x_j} - \frac{\partial p^r}{\partial x_i} + \frac{g}{\Theta}\theta^r \delta_{i3} + \nu \frac{\partial^2 u_i^r}{\partial x_j \partial x_j}, \tag{1.3}$$

where $\tau_{ij} = (u_i u_j)^r - u_i^r u_j^r$, p^r, Θ, ν and g are the SGS stress (the Leonard stress $L_{ij} = (u_i^r u_j^r)^r - u_i^r u_j^r$ has been included in τ_{ij}), the filtered kinematic pressure, the mean potential temperature, the kinematic viscosity and the gravitational acceleration, respectively, and the filtered resolvable-scale temperature equation,

$$\frac{\partial \theta^r}{\partial t} = -\frac{\partial \theta^r u_i^r}{\partial x_i} - \frac{\partial F_i}{\partial x_i} + \Gamma \frac{\partial^2 \theta^r}{\partial x_i^2}, \tag{1.4}$$

where $F_i = (u_i\theta)^r - u_i^r \theta^r$ and Γ are the SGS temperature flux and the molecular diffusivity, respectively, we have

$$\begin{aligned}\frac{\partial f}{\partial t} + v_j \frac{\partial f}{\partial x_j} = {} & \frac{\partial}{\partial v_i}\left\{\left\langle \frac{\partial \tau_{ij}}{\partial x_j} | \boldsymbol{u}^r = \boldsymbol{v}, \theta^r = \psi \right\rangle f\right\} + \frac{\partial}{\partial v_i}\left\{\left\langle \frac{\partial p^r}{\partial x_i} | \boldsymbol{u}^r = \boldsymbol{v}, \theta^r = \psi \right\rangle f\right\} \\ & - \frac{g}{\Theta}\frac{\partial}{\partial v_3}\{\langle \theta^r | \boldsymbol{u}^r = \boldsymbol{v}, \theta^r = \psi\rangle f\} + \frac{\partial}{\partial \psi}\left\{\left\langle \frac{\partial F_i}{\partial x_i} | \boldsymbol{u}^r = \boldsymbol{v}, \theta^r = \psi \right\rangle f\right\}.\end{aligned} \tag{1.5}$$

The two terms on the left-hand side are the time rate of change and advection in physical space. The first three terms on the right-hand side are transport in velocity space of the JPDF by the SGS stress divergence, the resolvable-scale pressure gradient and the buoyancy force, respectively. The last term is transport in temperature space by the SGS temperature–flux divergence. The viscous force and temperature diffusion terms are small and are omitted at high Reynolds numbers and high Péclet numbers.

Because SGS turbulence is often studied by analysing the SGS stress and flux rather than their divergences, an alternative form of the equation was given by Chen *et al.* (2005):

$$\begin{aligned}\frac{\partial f}{\partial t} + v_j \frac{\partial f}{\partial x_j} = {} & \frac{\partial^2}{\partial v_i \partial x_j}\{\langle \tau_{ij} | \boldsymbol{u}^r = \boldsymbol{v}, \theta^r = \psi\rangle f\} + \frac{\partial^2}{\partial v_i \partial v_j}\left\{\left\langle -\frac{1}{2} P_{ij} | \boldsymbol{u}^r = \boldsymbol{v}, \theta^r = \psi \right\rangle f\right\} \\ & + \frac{\partial^2}{\partial \psi \partial x_i}\{\langle F_i | \boldsymbol{u}^r = \boldsymbol{v}, \theta^r = \psi\rangle f\} + \frac{\partial^2}{\partial \psi \partial v_i}\{\langle -P_{F_i} | \boldsymbol{u}^r = \boldsymbol{v}, \theta^r = \psi\rangle f\} \\ & + \frac{\partial^2}{\partial \psi \partial \psi}\{\langle -P_\theta | \boldsymbol{u}^r = \boldsymbol{v}, \theta^r = \psi\rangle f\} + \frac{\partial^2}{\partial v_i \partial x_i}\{\langle p^r | \boldsymbol{u}^r = \boldsymbol{v}, \theta^r = \psi\rangle f\} \\ & + \frac{\partial^2}{\partial v_i \partial v_j}\left\{\left\langle p^r \frac{\partial u_j^r}{\partial x_i} | \boldsymbol{u}^r = \boldsymbol{v}, \theta^r = \psi \right\rangle f\right\} + \frac{\partial^2}{\partial v_i \partial \psi} \\ & \times \left\{\left\langle p^r \frac{\partial \theta^r}{\partial x_i} | \boldsymbol{u}^r = \boldsymbol{v}, \theta^r = \psi \right\rangle f\right\} - \frac{g}{\Theta}\frac{\partial}{\partial v_3}\{\langle \theta^r | \boldsymbol{u}^r = \boldsymbol{v}, \theta^r = \psi\rangle f\},\end{aligned} \tag{1.6}$$

where $P_{ij} = -\{\tau_{ik}(\partial u_j^r/\partial x_k) + \tau_{jk}(\partial u_i^r/\partial x_k)\}$, $P_{F_i} = -\{\tau_{ik}(\partial \theta^r/\partial x_k) + F_k(\partial u_i^r/\partial x_k)\}$ and $P_\theta = -F_i(\partial \theta^r/\partial x_i)$ are the SGS stress production rate, the SGS temperature flux production rate and the SGS temperature variance production rate, respectively. The terms on the right-hand side now are transport and mixed transport in velocity, physical and temperature spaces due to the SGS stress, the SGS stress production rate, the SGS temperature flux, the SGS temperature flux production

rate, the SGS temperature variance production rate, the resolvable-scale pressure, the pressure–strain correlation, the pressure–temperature-gradient correlation and the buoyancy force, respectively. The necessary conditions for LES to correctly predict the resolvable-scale velocity–temperature JPDF, therefore, are that the conditional SGS stress, the conditional SGS temperature flux, the conditional SGS stress production rate, and the conditional SGS temperature flux production rate, and the conditional SGS temperature variance production rate are reproduced by the SGS models (Chen *et al.* 2005). We emphasize that in addition to the SGS stress and flux, the SGS production terms, $\langle P_{ij}|\boldsymbol{u}^r = \boldsymbol{v}, \theta^r = \psi\rangle$, $\langle P_\theta|\boldsymbol{u}^r = \boldsymbol{v}, \theta^r = \psi\rangle$ and $\langle P_{F_i}|\boldsymbol{u}^r = \boldsymbol{v}, \theta^r = \psi\rangle$, directly affect the resolvable-scale velocity–temperature JPDF, while in traditional studies the importance of these production terms was not identified. The functional form of these conditional SGS statistics and their dependencies on the surface-layer dynamics are therefore of great importance for understanding the influence of the SGS turbulence and SGS models on the resolvable-scale statistics.

These conditions were used to study the dependencies of the resolvable-scale velocity–scalar JPDF on the SGS turbulence in a turbulent jet (Chen *et al.* 2005). The results show that the conditional SGS scalar flux and the conditional SGS scalar flux production rate have strong dependencies on the resolvable-scale velocity and scalar, indicating strong flow history effects. Chen & Tong (2006) investigated the SGS velocity field in the surface layer of the ABL and showed that the behaviours of the conditional SGS stress and the conditional SGS stress production rate are closely related to the surface layer dynamics, i.e. updrafts generated by buoyancy force, downdrafts associated with the large-scale convective eddies, the mean shear and the length-scale inhomogeneity in the vertical direction. In addition, they found that for updrafts, the conditional SGS stress and the conditional SGS stress production rate have similar trends, and their eigenvectors are generally well aligned, with the normalized tensorial contraction being close to unity, thereby indicating the potential of modelling the conditional SGS stress using its production rate.

In this work we investigate the effects of the SGS motions on the resolvable-scale velocity–temperature JPDF in unstable atmospheric surface layer and perform new *a priori* SGS model tests using measurement data. The field programme and the array filter technique for measuring resolvable- and subgrid-scale variables are given in § 2. Section 3 examines the measured conditional SGS statistics and the SGS model predictions. In addition to the conditional SGS temperature flux and the conditional SGS temperature flux production rate, we also examine the conditional SGS stress and the conditional SGS stress production rate because they also evolve the JPDF. The conclusions are given in § 4.

2. Measurement data

The field measurements, named the horizontal array turbulence study, or HATS field programme, were conducted at a field site near Kettleman City, California, in the summer of 2000 as a collaboration primarily among the National Center for Atmospheric Research, Johns Hopkins University, and Penn State University (C. T. was part of the Penn State group). Horst *et al.* (2004) describe the field site and the data collection procedures in detail. The field measurements used the design based on the transverse array technique proposed, studied and first used by the Penn State group (Edsall *et al.* 1995; Tong *et al.* 1997, 1998, 1999) for surface layer measurements in the ABL, which has been used subsequently by several groups in the ABL over land (Tong *et al.* 1997, 1999; Porté-Agel *et al.* 2001; Kleissl, Meneveau &

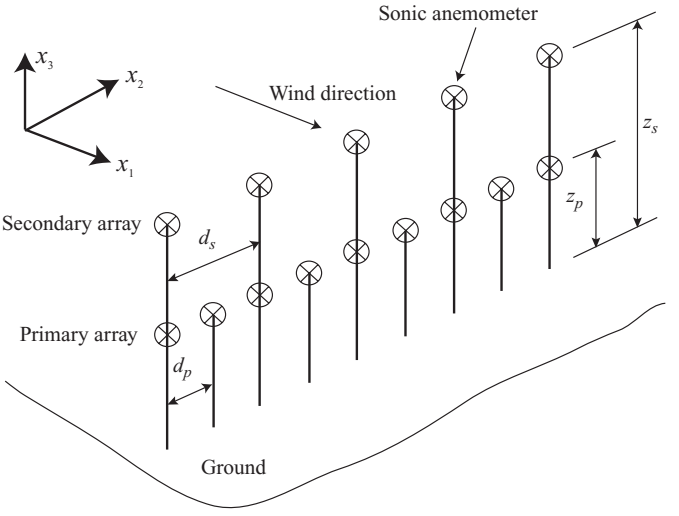

FIGURE 1. Schematic diagram of the array set-up. The secondary array (denoted by the subscript s) is used to obtain derivatives in the vertical direction. Note that for array 3, z_s is smaller than z_p and $d_s < d_p$.

Parlange 2003; Horst *et al.* 2004) and ocean (Kelly, Wyngaard & Sullivan 2009) as well as in engineering flows (Cerutti, Meneveau & Knio 2000; Tong 2001; Wang & Tong 2002; Chen *et al.* 2003; Rajagopalan & Tong 2003; Wang, Tong & Pope 2004). The technique uses horizontal sensor arrays (figure 1) aligned approximately perpendicular to the prevailing wind direction to perform two-dimensional filtering to obtain resolvable- and subgrid-scale variables. Two arrays are vertically spaced to obtain vertical derivatives.

The filter operation in the streamwise direction is performed by invoking Taylor's hypothesis. Filtering in the transverse direction is realized by averaging the output of the signals from the sensor array (Tong *et al.* 1998; Chen & Tong 2006). For example, the transversely filtered resolvable-scale velocity (denoted by the superscript t) is obtained as

$$u_i^t(\boldsymbol{x}, t) = \sum_{j=-N}^{N} C_j u_i(x_1, x_2 + j \times d, x_3, t), \tag{2.1}$$

where $2N+1$, C_j and d are the number of sensors on an array, the weighting coefficient for the jth sensor, and the spacing between adjacent sensors, respectively. We use $2N + 1 = 5$ and 3 for filtering at the heights of the primary and secondary arrays, respectively, to maintain the same filter size. In the present study we use the arrays to approximate top-hat filters, which are the most compact filter type in physical space. Because derivatives are computed using second-order finite differencing (with a spacing of $4d_p$ in the horizontal directions), which is effectively a top-hat filter, top-hat filters provide consistency among the resolvable-scale velocity and its derivatives. We average the outputs of five and three sonics to obtain the resolvable-scale variables for the primary and second arrays, respectively. The subgrid scales are obtained by subtracting the resolvable-scale part from the total variables. For more details refer to Chen & Tong (2006).

Array	Δ/z_p	z_p	d_p	z_s	d_s
1	3.88	3.45	3.35	6.90	6.70
2	2.00	4.33	2.167	8.66	4.33
3	1.00	8.66	2.167	4.33	1.08
4	0.48	4.15	0.50	5.15	0.625

TABLE 1. Configurations of the four arrays (lengths in metres).

Data	$\langle u \rangle$ ($\mathrm{m\,s^{-1}}$)	$-z/L$	u_* ($\mathrm{m\,s^{-1}}$)	ϵ ($\mathrm{m^2\,s^{-3}}$)	H ($\mathrm{K\,m\,s^{-1}}$)	χ_θ ($\mathrm{K^2\,s^{-1}}$)	Duration (min)
a	1.42	0.34	0.15	0.003	0.02	0.001	35
b	3.56	0.22	0.33	0.031	0.17	0.026	30
c	3.65	0.21	0.36	0.039	0.20	0.035	83
d	3.25	0.24	0.36	0.041	0.24	0.048	33

TABLE 2. Surface layer parameters for array 1 ($\Delta/z = 3.88$) under unstable conditions. The primary array height z_p is used for z. See § 3 for more details.

The array technique, including the accuracy of the array filter and the use of Taylor's hypothesis, has been systematically studied by Tong *et al.* (1998). They showed that a two-dimensional filter is a good approximation of a three-dimensional filter. Their analyses of the accuracy of a spectral cutoff array filter showed that the r.m.s. values of the filtered variables differ from that of a true spectral filter by less than 10 %. The accuracy of the top-hat filter array filter is expected to be higher (Chen & Tong 2006). The error associated with one-side finite differencing in the vertical direction was examined by Kleissl *et al.* (2003). They evaluated the divergence-free condition for the filter velocity field and concluded that reasonable accuracy can be achieved in computing derivatives of filtered velocity. Horst *et al.* (2004) further studied various issues of using the array technique including the aliasing errors associated with evaluating derivatives using finite differencing and furthermore demonstrated sufficient accuracy of the technique. Due to variations of the run-averaged wind direction, we rotate the coordinate system and interpolate the velocity and temperature in the Cartesian coordinate system defined by mean wind and cross-wind directions (Horst *et al.* 2004). The interpolation is performed in spectral space to avoid attenuating the high-frequency (wavenumber) fluctuations.

Four different array configurations, shown in table 1, are employed in the HATS programme. The filter aspect ratio (Δ/z) ranges from 0.48 to 3.88, allowing the effects of grid anisotropy to be examined, where Δ is the filter size ($=4d_p$). We refer to z as the height of the primary array z_p hereafter. Array 3 is at a much higher z; therefore, the effects of the stability parameter $-z/L$ can be examined, where $L = -(u_*^3\Theta)/(k_a g\langle u_3'\theta'\rangle)$, $u_*^2 = -\langle u_1'u_3'\rangle$ (the prime denotes fluctuations), and $k_a = 0.41$ (Pope 2000) are the Monin–Obukhov length, the square of the friction velocity and the von Kármán constant, respectively. The surface layer parameters for the data sets collected using the four arrays are given in tables 2 and 3. The results in Chen & Tong (2006) and in § 3.3 show that the SGS stress for array 1, which has the largest Δ/z, is the most anisotropic and most difficult for SGS models to predict; therefore, our discussions of results focus on array 1.

In this study we limit our scope to the unstable surface layer, i.e. cases with $z/L < 0$. All array 1 data used were collected during daytime under clear conditions with a Monin–Obukhov length of approximately −15 m. Ensemble averages are evaluated

Array	Δ/z ($\approx$)	$\langle u\rangle$ (m s^{-1})	$-z/L$	u_* (m s^{-1})	ϵ (m^2 s^{-3})	H (K m s^{-1})	χ_θ (K^2 s^{-1})	Total duration (min)
2	2.00	3.09	0.36	0.30	0.020	0.15	0.017	257
3	1.00	4.22	0.60	0.34	0.018	0.19	0.009	591
4	0.48	2.73	0.35	0.30	0.021	0.15	0.017	60

TABLE 3. Surface layer parameters for the other arrays under unstable conditions. The primary array height z_p is used for z.

Array	$\langle u_1'\theta'\rangle/H$	$\langle u_2'\theta'\rangle/H$	$\langle F_1\rangle/H$	$\langle F_2\rangle/H$	$\langle F_3\rangle/H$
1	−1.70	−0.23	−0.96	−0.00	0.70
2	−1.20	0.04	−0.62	0.02	0.56
3	−0.85	0.35	−0.26	0.01	0.33
4	−1.16	−0.21	−0.10	0.01	0.18

TABLE 4. Measured Reynolds-averaged temperature flux and the mean SGS temperature flux for the four arrays.

using time averages. Data sections that are quasi-stationary are generally 30–90 min in length. To achieve reasonable statistical convergence in our analysis, we combine the results of selected data sections collected under similar stability conditions using the each array configuration as done in Chen & Tong (2006). We normalize the results for each data set using its parameters, then weight-average them according to the number of conditional samples in each bin. The length of the combined data corresponds to approximately 10 000 advection time scales for the vertical-velocity energy-containing-scale eddies. Chen & Tong (2006) and Chen *et al.* (2009) have demonstrated that the data set is sufficient to achieve reasonable statistical convergence (typically less than 5 % of the maximum of the conditional statistics). This level of statistical uncertainties of the results is much smaller than the differences between the measurements and the SGS model predictions. In this paper we use the first-order kernel density estimation method (Wand & Jones 1995) to obtain the conditional statistics, achieving improved convergence and lower bias. We limit the results to the central part of the sample space that contains 99.9 % of the probability of the velocity–scalar JPDF.

3. Results

As in Chen & Tong (2006), we focus our discussions on results using data from array 1. The stability parameter, $-z/L$, has an average value of 0.24 for these data. Top-hat filters in both the streamwise and cross-stream directions are used to obtain the resolvable-scale and subgrid-scale variables with a filter size of $\Delta = 3.88z$, which is in the energy-containing range. The results for the other array configurations, i.e. different Δ/z, and $-z/L$ (table 3), are also obtained. They are generally similar to those for array 1 and are not discussed in detail. Table 4 gives the normalized Reynolds-averaged temperature flux and the ratios of the mean SGS temperature flux components to the vertical mean temperature flux. The SGS flux for array 1 has the largest fraction of the mean vertical temperature flux; therefore, it is the most challenging to SGS models. The measured and modelled SGS temperature flux components are given in table 5 and discussed in § 3.3.

All the results presented are normalized using the surface layer parameters. The conditional SGS stress, $\langle \tau_{ij} | \boldsymbol{u}^r, \theta^r \rangle$, and the conditional SGS stress production

	$\langle F_1\rangle/H$	$\langle F_2\rangle/H$	$\langle F_3\rangle/H$
F_i^{smg}	−0.003	−0.003	0.51
F_i^{nl}	−1.31	0.03	0.13
F_i^{mix}	−1.31	0.03	0.54

TABLE 5. Modelled mean SGS temperature flux for array 1.

rate, $\langle P_{ij}|\boldsymbol{u}^r,\theta^r\rangle$, are normalized by u_*^2 and the estimated energy dissipation rate, $\epsilon=\theta_\epsilon(u_*^3/k_az)$, respectively, where $\theta_\epsilon=1-z/L$ for $z/L\leqslant 0$, as suggested by Kaimal *et al.* (1972). The conditional SGS temperature flux, $\langle F_i|\boldsymbol{u}^r,\theta^r\rangle$, and the conditional SGS temperature flux production rate, $\langle P_{F_i}|\boldsymbol{u}^r,\theta^r\rangle$, are normalized by the mean vertical heat flux, $H=\langle\theta' u_3'\rangle$, and $-T_*u_*^2/z$, respectively, where the prime denotes fluctuations and $T_*=-H/u_*$ is the scale for temperature fluctuations. The conditional SGS variance spectral transfer rate, $\langle P_\theta|\boldsymbol{u}^r,\theta^r\rangle$, is normalized by the estimated temperature variance transfer rate, $\chi_\theta=\theta_h(T_*^2u_*/k_az)$, where $\theta_h=0.74\times(1-9z/L)^{-1/2}$ for $z/L\leqslant 0$, as suggested by Businger *et al.* (1971).

3.1. *Conditional SGS temperature flux and conditional SGS temperature flux production rate*

The results for the conditional SGS temperature flux components $\langle F_1|\boldsymbol{u}^r,\theta^r\rangle$, $\langle F_2|\boldsymbol{u}^r,\theta^r\rangle$ and $\langle F_3|\boldsymbol{u}^r,\theta^r\rangle$ are shown in figure 2. For convenience, we omit the sample-space variables $\boldsymbol{v}$ and ψ from the conditional means here and hereafter. In addition, only the fluctuating parts of $\boldsymbol{u}^r$ and θ^r normalized by their respective r.m.s. values are plotted.

The results show that $\langle F_1|\boldsymbol{u}^r,\theta^r\rangle$ and $\langle F_3|\boldsymbol{u}^r,\theta^r\rangle$ depend strongly on u_1^r and u_3^r for positive and small θ^r fluctuations, and the dependencies are weaker for negative θ^r fluctuations. The lateral SGS flux, $\langle F_2|\boldsymbol{u}^r,\theta^r\rangle$, also depends on $|u_2^r|$ and u_3^r for positive and small θ^r fluctuations, and the dependence is weaker for negative θ^r fluctuations. Generally, $\langle F_1|\boldsymbol{u}^r,\theta^r\rangle$ has larger values compared to the other components, probably because large temperature fluctuations are highly correlated with the streak structure in the surface layer, resulting in a large flux. The trends of the conditional SGS temperature flux production rate (figure 3) generally are similar to those of the conditional SGS flux for positive and small θ^r fluctuations, suggesting that the former has a strong influence on the evolution of the latter. The dependencies on the resolvable-scale velocity for negative θ^r fluctuations are weak.

To better understand the relationship between the conditional SGS temperature flux and its production rate, we expand $\langle P_{F_1}|\boldsymbol{u}^r,\theta^r\rangle$ as

$$\langle P_{F_1}|\boldsymbol{u}^r,\theta^r\rangle=-\left\langle F_1\frac{\partial u_1^r}{\partial x_1}+F_2\frac{\partial u_1^r}{\partial x_2}+F_3\frac{\partial u_1^r}{\partial x_3}+\tau_{11}\frac{\partial\theta^r}{\partial x_1}+\tau_{12}\frac{\partial\theta^r}{\partial x_2}+\tau_{13}\frac{\partial\theta^r}{\partial x_3}|\boldsymbol{u}^r,\theta^r\right\rangle. \tag{3.1}$$

The first three terms on the right-hand side are the production rate due to the interaction between the SGS temperature flux and the resolvable-scale velocity gradient and the last three terms are the production rate due to the interaction between the SGS stress and the resolvable-scale temperature gradient. Our results show that the leading components in $\langle P_{F_1}|\boldsymbol{u}^r,\theta^r\rangle$ are $\langle -F_3(\partial u_1^r/\partial x_3)|\boldsymbol{u}^r,\theta^r\rangle$ and $\langle -\tau_{13}(\partial\theta^r/\partial x_3)|\boldsymbol{u}^r,\theta^r\rangle$, which have similar trends and magnitudes, therefore are the focus of our discussion. The rest of the terms are relatively small because the

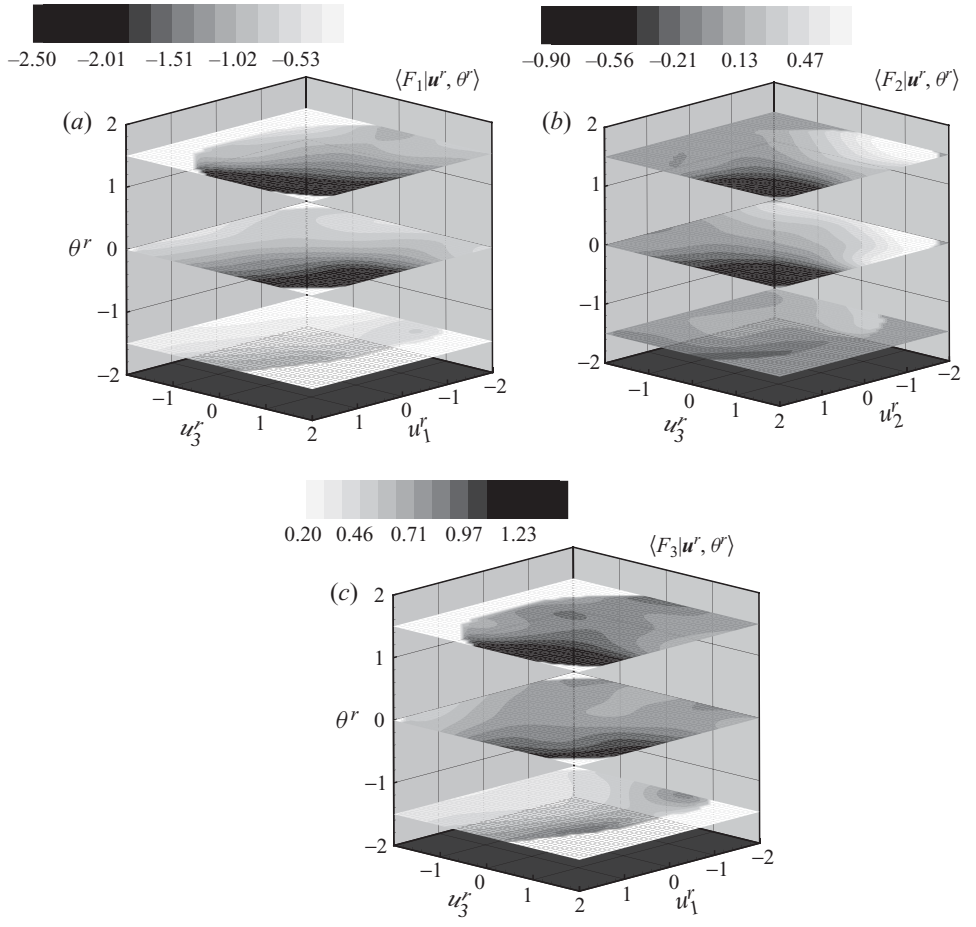

FIGURE 2. Conditional SGS temperature flux. The dependencies on the resolvable-scale velocity are strong for positive θ^r and are weak for negative θ^r.

horizontal derivatives of u_1^r and θ^r are relatively small compared with their vertical derivatives in the surface layer. Similarly, $\langle P_{F_3}|\boldsymbol{u}^r, \theta^r\rangle$ can be expanded as:

$$\langle P_{F_3}|\boldsymbol{u}^r, \theta^r\rangle = -\left\langle F_1\frac{\partial u_3^r}{\partial x_1} + F_2\frac{\partial u_3^r}{\partial x_2} + F_3\frac{\partial u_3^r}{\partial x_3} + \tau_{31}\frac{\partial \theta^r}{\partial x_1} + \tau_{32}\frac{\partial \theta^r}{\partial x_2} + \tau_{33}\frac{\partial \theta^r}{\partial x_3}|\boldsymbol{u}^r, \theta^r\right\rangle. \tag{3.2}$$

The dominant component in $\langle P_{F_3}|\boldsymbol{u}^r, \theta^r\rangle$ is $\langle -\tau_{33}(\partial\theta^r/\partial x_3)|\boldsymbol{u}^r, \theta^r\rangle$, because the derivatives of u_3^r and θ^r in the horizontal directions are relatively small. Our attention, therefore, is focused on $\langle -\tau_{33}(\partial\theta^r/\partial x_3)|\boldsymbol{u}^r, \theta^r\rangle$.

We now discuss the trends for $\langle P_{F_1}|\boldsymbol{u}^r, \theta^r\rangle$ and $\langle P_{F_3}|\boldsymbol{u}^r, \theta^r\rangle$. For positive θ^r fluctuations, the eddies associated with updrafts generally come from the region near the ground, and have smaller length scales, thereby containing large magnitudes of the vertical SGS flux and the SGS stress. They are also likely to have experienced strong shear and vertical temperature gradient. Thus, F_3, τ_{33} and $\partial u_1^r/\partial x_3$ have large positive values while τ_{13} and $\partial\theta^r/\partial x_3$ have large negative values, resulting in negative $\langle -F_3(\partial u_1^r/\partial x_3)|\boldsymbol{u}^r, \theta^r\rangle$ and $\langle -\tau_{13}(\partial\theta^r/\partial x_3)|\boldsymbol{u}^r, \theta^r\rangle$, and positive $\langle -\tau_{33}(\partial\theta^r/\partial x_3)|\boldsymbol{u}^r, \theta^r\rangle$.

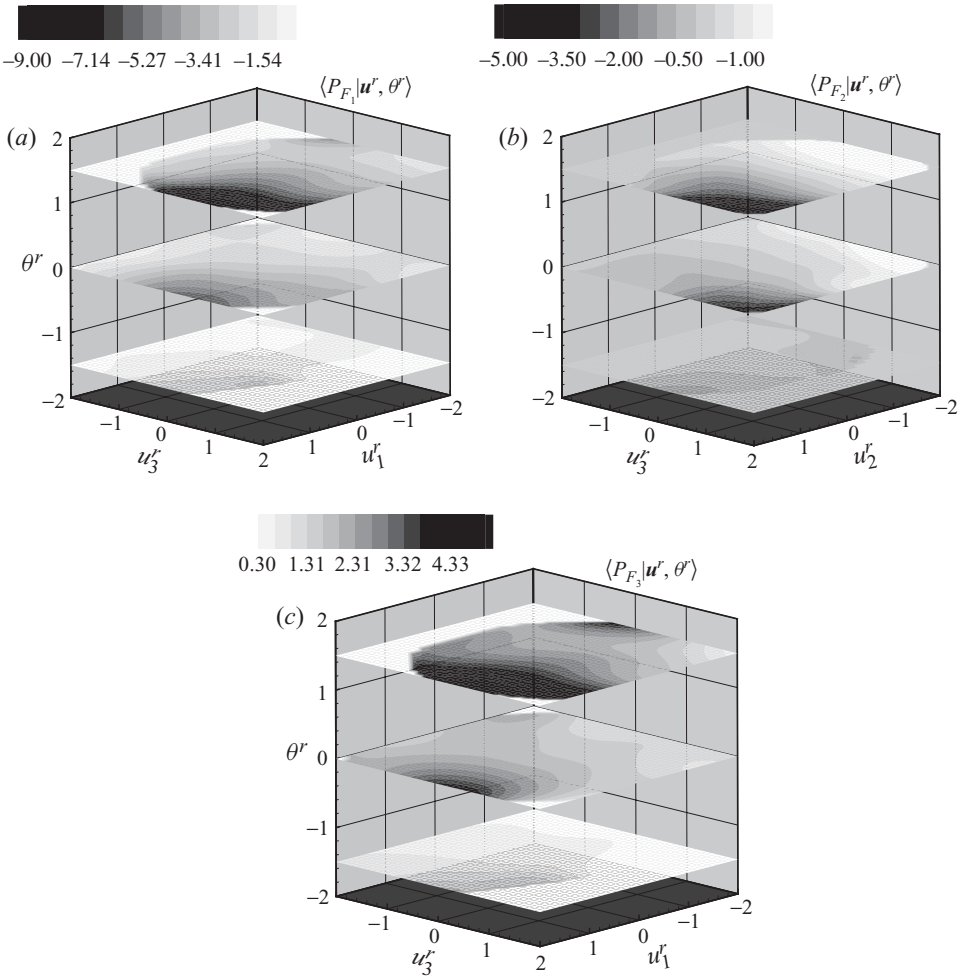

FIGURE 3. Conditional SGS temperature flux production rate.

Because the vertical shear, the vertical flux and the vertical temperature gradient are larger for positive values of u_1^r and u_3^r, the magnitudes of $\langle P_{F_1}|\boldsymbol{u}^r, \theta^r\rangle$ and $\langle P_{F_3}|\boldsymbol{u}^r, \theta^r\rangle$ increase with u_1^r and u_3^r. For small θ^r fluctuations, the eddies are generally well mixed; therefore, they tend to be more symmetric in the vertical direction, as reflected by the symmetry of the conditional means of $\partial u_1^r/\partial x_3$ and $\partial\theta^r/\partial x_3$ (not shown) respective to u_3^r. Consequently, the magnitudes of $\langle P_{F_1}|\boldsymbol{u}^r, \theta^r\rangle$ and $\langle P_{F_3}|\boldsymbol{u}^r, \theta^r\rangle$ increase with u_1^r and u_3^r. For negative θ^r fluctuations, the eddies associated with downdrafts generally come from the mixed-layer region and carry relatively small amounts of SGS flux (figure 2*c*); therefore, the magnitudes of $\langle P_{F_1}|\boldsymbol{u}^r, \theta^r\rangle$ and $\langle P_{F_3}|\boldsymbol{u}^r, \theta^r\rangle$ are small and have weak dependencies on the resolvable-scale velocity.

Comparing the results for the different θ^r values, the location of the highest value of the conditional SGS temperature flux production rate appears to shift towards positive u_3^r when θ^r increases, probably because $\langle \partial u_1^r/\partial x_3|\boldsymbol{u}^r, \theta^r\rangle$ and $\langle \partial\theta^r/\partial x_3|\boldsymbol{u}^r, \theta^r\rangle$ are enhanced by both updrafts with high temperature (positive θ^r fluctuations) and downdrafts with low temperature (negative θ^r fluctuations).

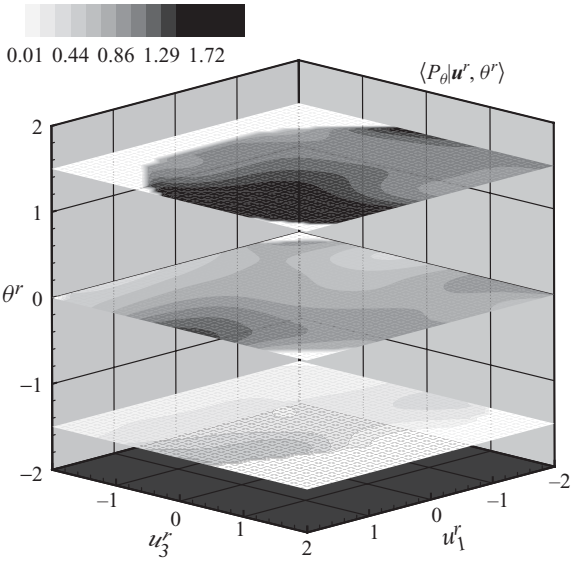

FIGURE 4. Conditional SGS temperature variance production rate.

Chen & Tong (2006) observed that the conditional SGS stress and the conditional SGS stress production rate have similar trends for positive u_3^r, which they argued to be the result of the approximate balance between the SGS stress production rate and the pressure destruction rate and the fact that the pressure destruction rate can be modelled as τ_{ij}/t_Δ, where t_Δ is an integral time scale. The similar trends between the conditional SGS temperature flux and the conditional SGS temperature flux production rate for positive θ^r fluctuations probably also reflect a balance between the production rate and the pressure destruction rate as well as the validity of using the ratio of the SGS temperature flux to a time scale to model the pressure destruction. The differences between the trends of the conditional SGS temperature flux and the conditional SGS temperature flux production rate for small and negative θ^r fluctuations are probably an indication that the production rate is small and no longer balances the pressure destruction rate.

The dominant components in $\langle P_{F_1}|\boldsymbol{u}^r,\theta^r\rangle$ contain a 'slow' term $\langle -F_3(\partial u_1^r/\partial x_3)|\boldsymbol{u}^r,\theta^r\rangle$ (it does not respond instantly to changes in the temperature gradient), in which F_3 influences $\langle P_{F_1}|\boldsymbol{u}^r,\theta^r\rangle$ through the interaction with $\partial u_1^r/\partial x_3$ (the F_1 component, however, does not directly affect $\langle P_{F_3}|\boldsymbol{u}^r,\theta^r\rangle$, which is dominated by $\langle \tau_{33}(\partial\theta^r/\partial x_3)|\boldsymbol{u}^r,\theta^r\rangle$). Consequently, in LES poor predictions of the vertical SGS temperature flux component by an SGS model may result in inaccuracies in the horizontal resolvable-scale temperature flux. In addition, because $\langle -\tau_{13}(\partial\theta^r/\partial x_3)|\boldsymbol{u}^r,\theta^r\rangle$ affects $\langle P_{F_1}|\boldsymbol{u}^r,\theta^r\rangle$ due to the dominant vertical derivative of resolvable-scale temperature, underpredictions of the conditional SGS shear stress components might also result in inaccuracies in the resolvable-scale horizontal temperature flux in an LES.

3.2. *SGS temperature variance production rate*

The SGS temperature variance production rate $\langle P_\theta|\boldsymbol{u}^r,\theta^r\rangle$ (figure 4) generally increases with u_1^r and u_3^r. This dependence is strong for positive θ^r fluctuations and weak for negative θ^r fluctuations. The dominant component of $\langle P_\theta|\boldsymbol{u}^r,\theta^r\rangle$ is $\langle F_3(\partial\theta^r/\partial x_3)|\boldsymbol{u}^r,\theta^r\rangle$. Because both F_3 and $\partial\theta^r/\partial x_3$ increase with u_1^r and u_3^r for positive

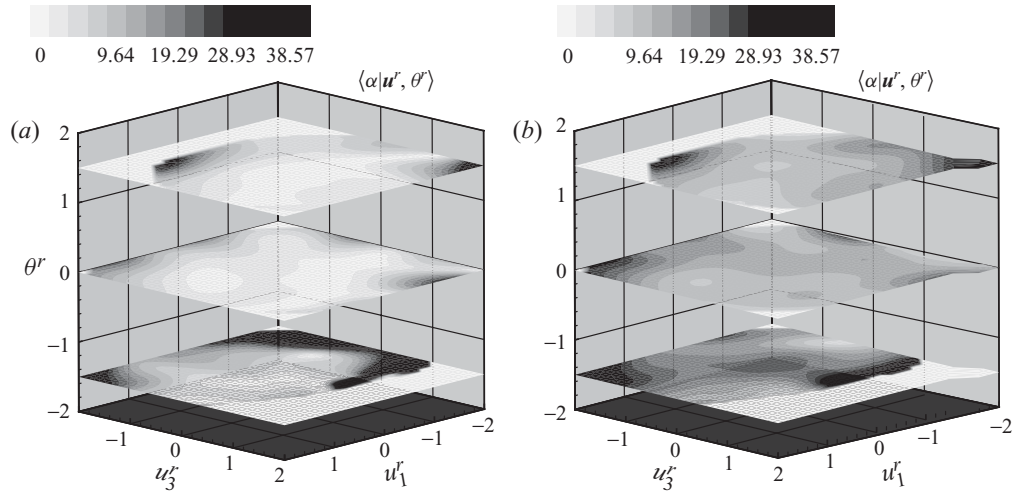

FIGURE 5. (*a*) Geometric alignment angle between the measured conditional SGS temperature flux and the conditional SGS stress production rate. The alignment angle is small for positive u_3^r and θ^r and is larger for negative u_3^r and θ^r. (*b*) The buoyancy production is included. The alignment angle is similar to that in (*a*).

θ^r, so does $\langle P_\theta|\boldsymbol{u}^r,\theta^r\rangle$. The asymmetry with respect to θ^r is likely the main cause of the positive skewness for θ^r and θ in the surface layer, which our data show to be approximately 0.34 and 0.58, respectively. The positive temperature skewness is related to rising plumes, and is a driving force for the positive skewness for both u_3^r and u_3 (0.22 and 0.4 respectively) observed in the present work and in previous studies (Lenschow & Stephens 1980; Wyngaard 1988). Because higher temperatures cause rising plumes, the skewness value for the temperature is larger than that for the vertical velocity. Chen & Tong (2006) and Chen *et al.* (2009) argued that an underprediction of the asymmetry of $\langle P_{33}|u_3^r\rangle$ causes underprediction of the u_3^r skewness (e.g. Moeng 1984; Chen *et al.* 2009). The SGS model predictions of $\langle P_\theta|\boldsymbol{u}^r,\theta^r\rangle$ will be examined in § 3.7.

3.3. *Alignment between SGS temperature flux and its production rate*

Chen & Tong (2006) observed that the anisotropic parts of $\langle\tau_{ij}|\boldsymbol{u}^r\rangle$ and $\langle P_{ij}|\boldsymbol{u}^r\rangle$ have similar trends, and their eigenvectors are well aligned with their normalized tensorial contraction close to unity for positive u_3^r, again indicating the balance between the production rate and the pressure destruction rate and the validity of using the SGS stress and a time scale to model the pressure destruction rate. The results in § 3.1 also show that $\langle F_i|\boldsymbol{u}^r,\theta^r\rangle$ and $\langle P_{F_i}|\boldsymbol{u}^r,\theta^r\rangle$ have similar trends. To investigate the relationship between $\langle F_i|\boldsymbol{u}^r,\theta^r\rangle$ and $\langle P_{F_i}|\boldsymbol{u}^r,\theta^r\rangle$, we compute the alignment angle between $\langle F_i|\boldsymbol{u}^r,\theta^r\rangle$ and $\langle P_{F_i}|\boldsymbol{u}^r,\theta^r\rangle$, which is given by

$$\alpha=\cos^{-1}\left(\frac{|\langle F_i|\boldsymbol{u}^r,\theta^r\rangle\langle P_{F_i}|\boldsymbol{u}^r,\theta^r\rangle|}{|\langle F_i|\boldsymbol{u}^r,\theta^r\rangle||\langle P_{F_i}|\boldsymbol{u}^r,\theta^r\rangle|}\right). \tag{3.3}$$

Figure 5 shows that $\langle F_i|\boldsymbol{u}^r,\theta^r\rangle$ and $\langle P_{F_i}|\boldsymbol{u}^r,\theta^r\rangle$ are generally well aligned with the alignment angle, α, generally less than 10° for positive and small θ^r fluctuations. For negative θ^r fluctuations, the alignment angle is small for positive u_3^r and is larger (but still less than 30°) for negative u_3^r. This trend is similar to the alignment property for the conditional SGS stress and its production rate (Chen & Tong 2006) and is

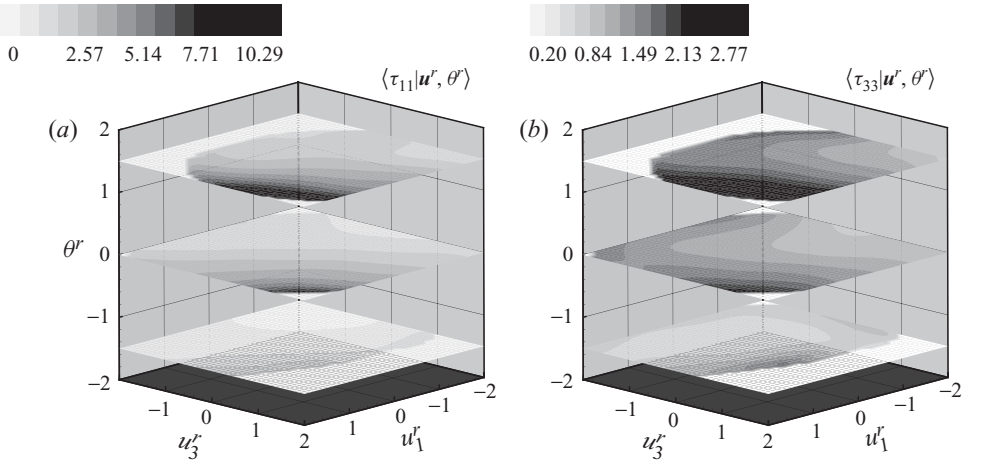

FIGURE 6. Conditional SGS normal stress. The dependencies are strong for positive θ^r and weak for negative θ^r.

probably because $\langle P_{F_i}|\boldsymbol{u}^r, \theta^r\rangle$ is small and might no longer be a dominant term in the SGS flux transport equation, therefore not in balance with the pressure destruction. In addition, it might not be appropriate to model the pressure destruction term as the ratio of the SGS flux to a time scale under this condition.

We also examine the effects of buoyancy force on the alignment property by including the buoyancy production term ($P_{F_B} = (g/\Theta)[(\theta^2)^r - (\theta^r)^2]$) in the SGS temperature flux production rate. The alignment angle (figure 5*b*) only increases slightly, indicating that buoyancy does not significantly alter the alignment property. These results are consistent with the similarity between the conditional SGS temperature flux and the conditional SGS temperature flux production rate, suggesting a balance between the production rate and the pressure destruction rate and the validity of using the SGS temperature flux and a time scale for modelling the pressure destruction for positive θ^r fluctuations.

In the present work the alignment between the conditional SGS temperature flux and the conditional SGS flux production rate is studied in the context of the velocity–temperature JPDF equation. Previous studies (e.g. Higgins, Meneveau & Parlange 2007) have examined the alignment properties of the instantaneous SGS heat flux and the instantaneous resolvable-scale gradient. While the alignment properties of these instantaneous vectors are not related to the JPDF equation, the alignment between the instantaneous SGS flux and the SGS flux production rate will be helpful to understand the results in the present study. This issue will be addressed in a separate paper.

3.4. *Conditional SGS stress and conditional SGS stress production rate*

The normalized conditional SGS stress components, $\langle \tau_{11}|\boldsymbol{u}^r, \theta^r\rangle$ and $\langle \tau_{33}|\boldsymbol{u}^r, \theta^r\rangle$, are given in figure 6. The results show that similar to the SGS temperature flux, $\langle \tau_{11}|\boldsymbol{u}^r, \theta^r\rangle$ and $\langle \tau_{33}|\boldsymbol{u}^r, \theta^r\rangle$ generally increase with u_1^r and u_3^r. The dependence on the velocity is strong for positive θ^r fluctuations and is weak for negative θ^r fluctuations.

The conditional SGS stress production rate $\langle P_{11}|\boldsymbol{u}^r, \theta^r\rangle$ (figure 7*a*) has a similar trend to $\langle \tau_{11}|\boldsymbol{u}^r, \theta^r\rangle$ (figure 6*a*), suggesting that there is a local conditional balance between the SGS stress production rate and the pressure destruction rate. The trend of $\langle P_{33}|\boldsymbol{u}^r, \theta^r\rangle$ (figure 7*b*), however, is different from $\langle \tau_{33}|\boldsymbol{u}^r, \theta^r\rangle$ (figure 6*b*), because

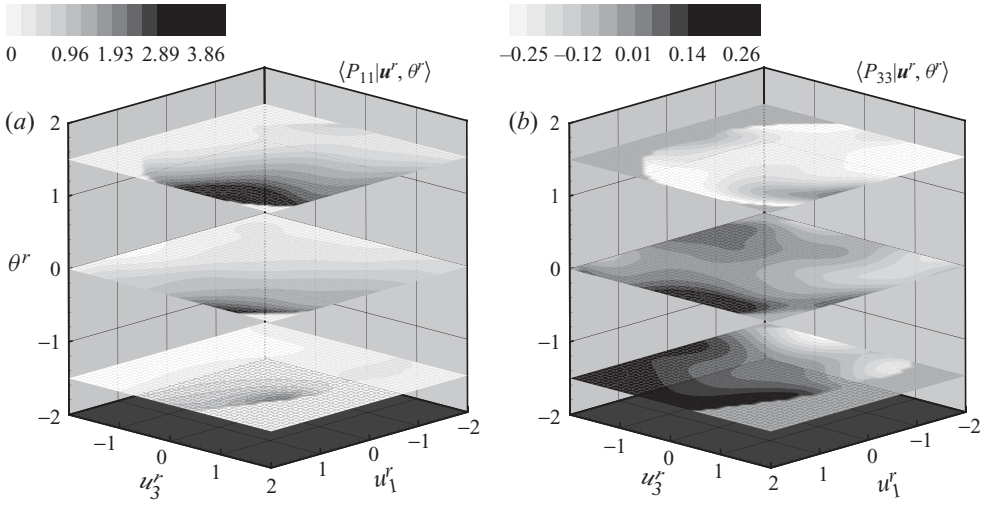

FIGURE 7. Conditional means of the normal components of the SGS stress production rates.

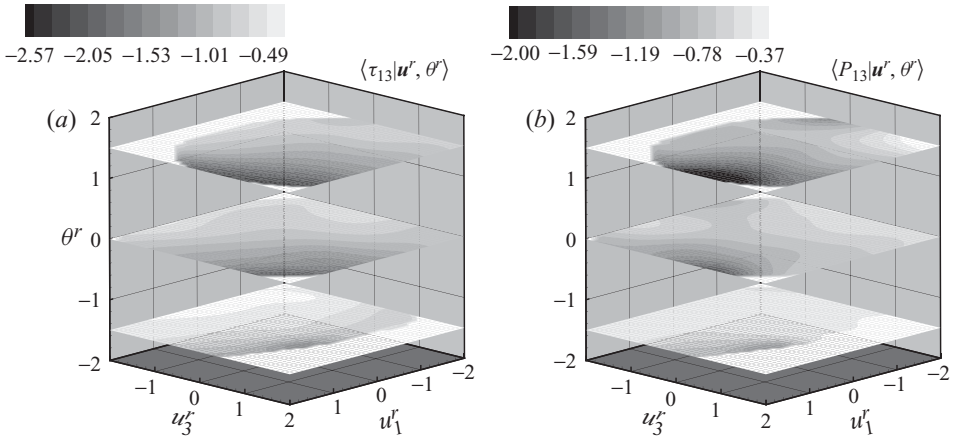

FIGURE 8. Conditional SGS shear stress and the off-diagonal component of the SGS stress production rate.

the buoyancy production rate dominates the evolution of $\langle \tau_{33}|\boldsymbol{u}^r, \theta^r\rangle$, consistent with our previous results (Chen & Tong 2006).

The production rate component $\langle P_{33}|\boldsymbol{u}^r, \theta^r\rangle$ has negative values for positive θ^r fluctuations, indicating that τ_{33} loses energy to τ_{11} and τ_{22}, and there is conditional backscatter. For negative θ^r fluctuations, $\langle P_{33}|\boldsymbol{u}^r, \theta^r\rangle$ is positive, indicating that τ_{33} gains energy. Our previous study (Chen & Tong 2006) has shown that an underprediction of the dependence of $\langle P_{33}|\boldsymbol{u}^r, \theta^r\rangle$ on u_3^r will cause the same for the vertical-velocity skewness.

The conditional shear stress production rate, $\langle P_{13}|\boldsymbol{u}^r, \theta^r\rangle$, (figure 8*b*) has a similar trend to $\langle \tau_{13}|\boldsymbol{u}^r, \theta^r\rangle$ (figure 8*a*), again indicating conditional equilibrium. Our previous study (Chen & Tong 2006) has shown that underpredictions of the trend and magnitude of τ_{13} cause an overprediction of the mean streamwise velocity gradient near the surface, and that the correct prediction of $\langle \tau_{13}|\boldsymbol{u}^r\rangle$ is very important for predicting the horizontal velocity variance profile.

We note that the dependence of $\langle \tau_{ij} | \boldsymbol{u}^r, \theta^r \rangle$ on θ^r reflects partly the flow history effect and partly the buoyancy effect. A velocity field is not affected by a passive scalar. This property, however, does not preclude any dependence of velocity statistics on the scalar. The dependencies of the conditional SGS stress and the conditional SGS stress production rate on the resolvable-scale scalar can result from the different flow histories that the SGS eddies with the same resolvable-scale velocity but different resolvable-scale scalar values have experienced, as shown by the results obtained in a turbulent jet with passive temperature fluctuations (Chen *et al.* 2005). In the convective ABL studied, the potential temperature is not passive. Hence, buoyancy plays a role. The observed dependencies on the potential temperature, therefore, are partly due to the flow history and partly due to the buoyancy effects. To investigate the influence of the buoyancy on the dependencies, a passive scalar needs to be introduced into the surface layer with a similar lower boundary condition (constant flux). The HATS programme did not include such a passive scalar. It would be interesting to study this issue using simulations (i.e. high-resolution LES).

3.5. *Anisotropy of the conditional SGS stress*

An important property of the SGS stress is its level of anisotropy. The level of anisotropy of the conditional SGS stress can be characterized using the Lumley triangle (Lumley 1978). The dependence of the anisotropy on the resolvable-scale velocity (Lumley triangle for $\langle \tau_{ij} | \boldsymbol{u}^r \rangle$) was studied in Chen & Tong (2006), which shows that the anisotropy is weak for negative u_3^r and strong for positive u_3^r. For positive and negative u_1^r values, $\langle \tau_{ij} | \boldsymbol{u}^r \rangle$ is close to axisymmetric with one large and one small eigenvalue, respectively, likely reflecting the shear and buoyancy effects. Here we study the dependence of the anisotropy on the resolvable-scale temperature. The normalized anisotropy tensor for $\langle \tau_{ij} | \boldsymbol{u}^r, \theta^r \rangle$, $(\langle \tau_{ij} | \boldsymbol{u}^r, \theta^r \rangle / \langle \tau_{kk} | \boldsymbol{u}^r, \theta^r \rangle) - \delta_{ij}/3$, can be determined by two variables ξ and η defined in terms of its invariants (Pope 2000):

$$6\eta^2 = -2II = \frac{\langle \tau_{ij}^d | \boldsymbol{u}^r, \theta^r \rangle \langle \tau_{ij}^d | \boldsymbol{u}^r, \theta^r \rangle}{\langle \tau_{kk} | \boldsymbol{u}^r, \theta^r \rangle^2} \tag{3.4}$$

and

$$6\xi^3 = 3III = \frac{\langle \tau_{ij}^d | \boldsymbol{u}^r, \theta^r \rangle \langle \tau_{jk}^d | \boldsymbol{u}^r, \theta^r \rangle \langle \tau_{ki}^d | \boldsymbol{u}^r, \theta^r \rangle}{\langle \tau_{kk} | \boldsymbol{u}^r, \theta^r \rangle^3}, \tag{3.5}$$

where $\tau_{ij}^d = \tau_{ij} - \tau_{kk}\delta_{ij}/3$ is the deviatoric part of the SGS stress, and II and III are the second and third invariants of the anisotropy tensor, respectively. If $\langle \tau_{ij} | \boldsymbol{u}^r, \theta^r \rangle$ is isotropic, both ξ and η are zero. (The first invariant or trace of $\langle \tau_{ij}^d | \boldsymbol{u}^r, \theta^r \rangle$ is always zero by definition.) The Lumley triangle representation for the conditional SGS stress is shown in figure 9. The arrows represent the conditioning velocity vectors (see Chen & Tong 2006 for more details). The results show that there is a clear dependence of the anisotropy on the resolvable-scale temperature. For positive and small θ^r fluctuations, $\langle \tau_{ij} | u_1^r, u_3^r, \theta^r \rangle$ is quite anisotropic and close to the results for $\langle \tau_{ij} | u_1^r, u_3^r \rangle$ (without conditioning on θ^r), consistent with the trends of $\langle \tau_{ij} | \boldsymbol{u}^r, \theta^r \rangle$ in § 3.4. The points representing the anisotropy are not far from $\eta = -\xi$ and $\eta = \xi$, indicating that $\langle \tau_{ij} | u_1^r, u_3^r, \theta^r \rangle$ is close to axisymmetric with either one small eigenvalue or one large eigenvalue. One difference between the results for small θ^r fluctuations and for positive θ^r fluctuations is that there are more points close to $\eta = \xi$ than $\eta = -\xi$ for the former, indicating that the SGS eddies are more likely to contain SGS stress that is close to axisymmetric with one large eigenvalue. This trend is probably

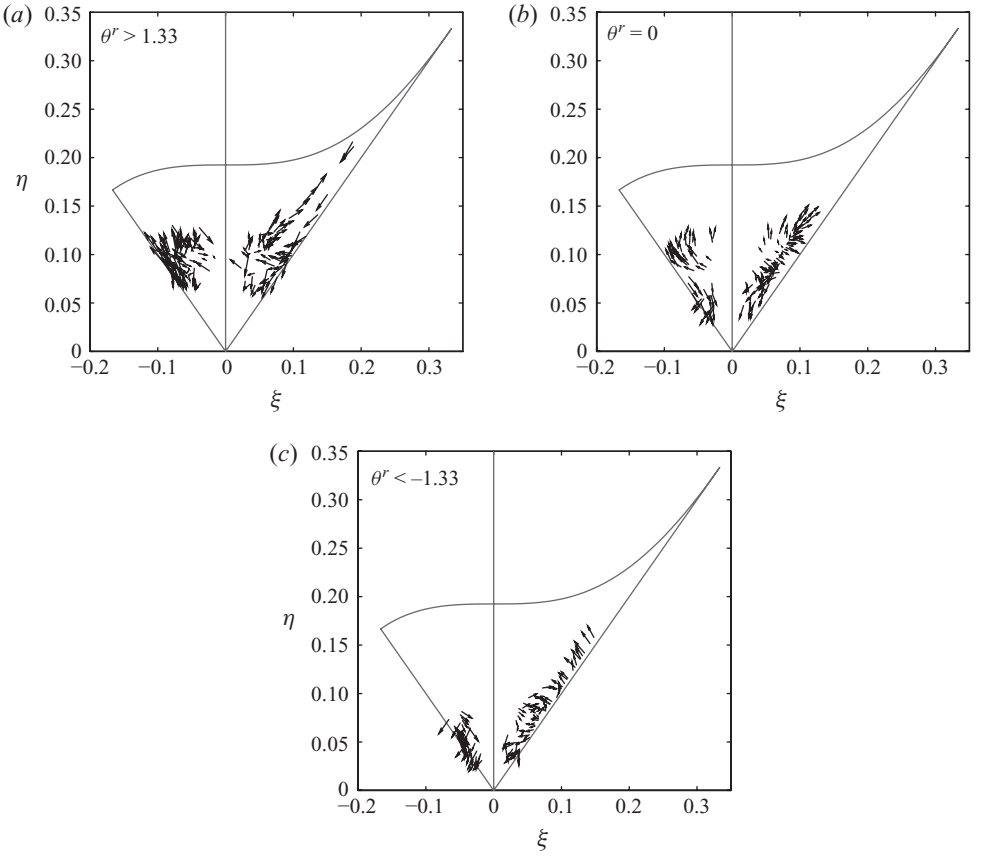

FIGURE 9. The Lumley triangle representation of the conditional SGS stress. The arrows represent the conditioning vectors (u_1^r, u_3^r). (*a*) Positive θ^r. The conditional SGS stress, $\langle \tau_{ij} | u_1^r, u_3^r, \theta^r \rangle$, is quite anisotropic and close to the results for $\langle \tau_{ij} | u_1^r, u_3^r \rangle$ (without conditioning on θ^r). (*b*) Small θ^r. The results are similar to (*a*). (*c*) Negative θ^r. The conditional SGS stress is less anisotropic.

because in the former case the compression and shear effects are weakened as these eddies are likely to have gone through a strong mixing process.

For negative θ^r fluctuations, there are more points representing the anisotropy close to the origin than for positive and small θ^r fluctuations, indicating a somewhat less anisotropic SGS stress. In addition, some points with $u_3^r < 0$ are close to axisymmetric with one small eigenvalue ($\eta = -\xi$) due to the compression effects associated with the returning flow of the large convective eddies. On the other hand, some points with $u_3^r > 0$ are close to the axisymmetric with one large eigenvalue ($\eta = \xi$) due to the weakened shear effect.

The results discussed above are for $\Delta/z = 3.88$ and $-z/L = 0.24$ (array 1). The level of the anisotropy of $\langle \tau_{ij} | u_1^r, u_3^r, \theta^r \rangle$ for different array configurations is shown in figure 10. For positive θ^r fluctuations, the results for $\langle \tau_{ij} | u_1^r, u_3^r, \theta^r \rangle$ are similar to those for $\langle \tau_{ij} | u_1^r, u_3^r \rangle$ (i.e. without conditional on θ^r) discussed in Chen & Tong (2006). The results of $\langle \tau_{ij} | u_1^r, u_3^r, \theta^r > 1.33 \rangle$ for different array configurations are qualitatively similar to those for array 1. A comparison between the levels of anisotropy for arrays 2 and 4 (fixing $-z/L$ and reducing Δ/z from 2.00 for array 2 to 0.48 for array 4) shows that there are fewer points for the axisymmetric SGS stress with one small eigenvalue

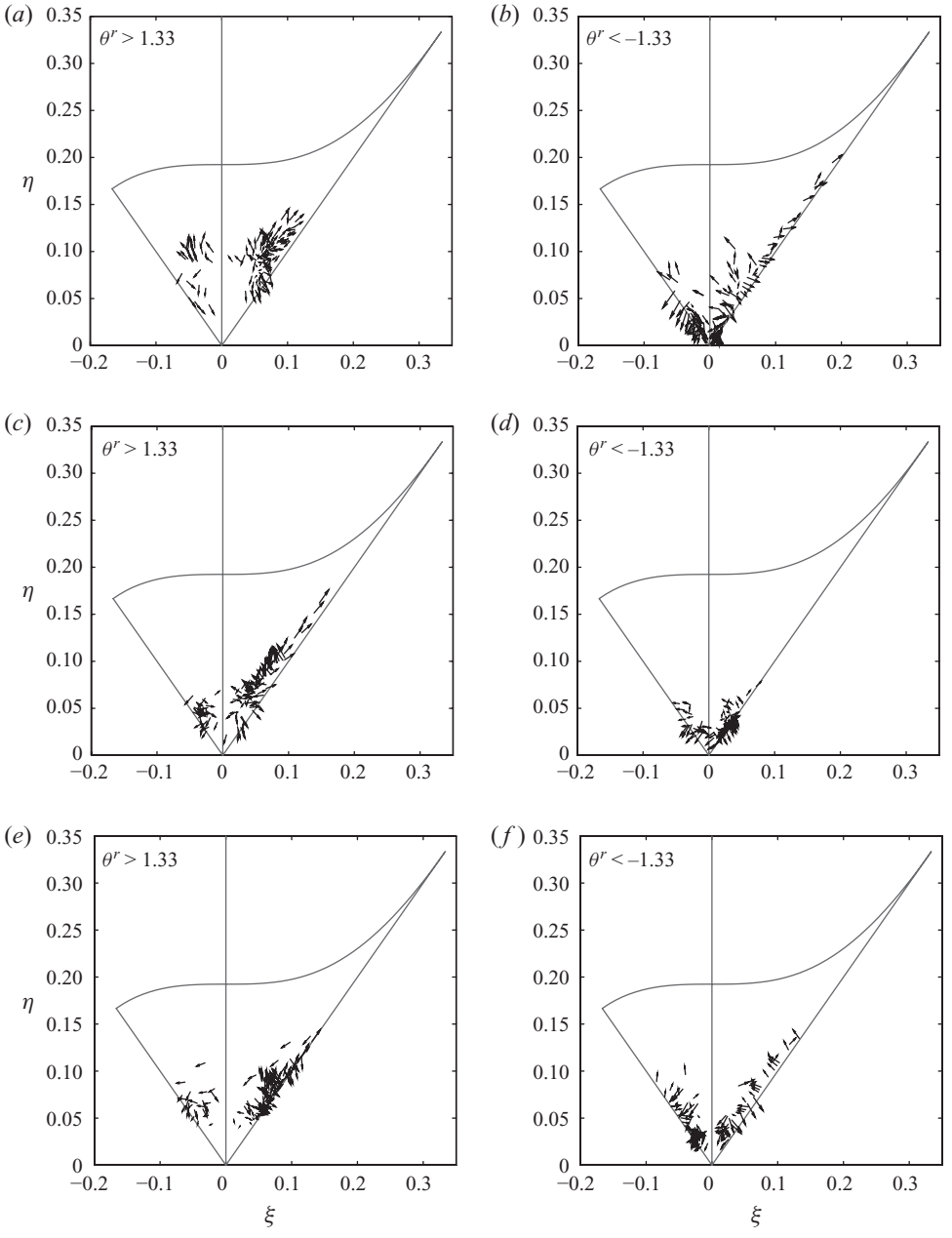

FIGURE 10. The Lumley triangle representation of the conditional SGS stress for the other array configurations: (*a*, *b*) array 2 ($\Delta/z = 2.00, -z/L = 0.36$); (*c*, *d*) array 3 ($\Delta/z = 1.00$, $-z/L = 0.60$); (*e*, *f*) array 4 ($\Delta/z = 0.48, -z/L = 0.35$).

($\eta = -\xi$) for array 4 than for array 2. This trend is likely because the measured compression effects associated with the returning flow of large convective eddies are weaker for array 4 than for array 2. A comparison between the levels of anisotropy for array 2 ($\Delta/z = 2.00, -z/L = 0.36$) and array 3 ($\Delta/z = 1.00, -z/L = 0.60$) shows that $\langle \tau_{ij} | u_1^r, u_3^r \rangle$ for array 3 is less anisotropic than that for array 2, and has very few points near the line of axisymmetric SGS stress with one small eigenvalue ($\eta = -\xi$).

These trends are because of the enhanced buoyancy effect due to the larger $-z/L$ value and the weaker shear and compression effects due to the smaller Δ/z. The level of the anisotropy of $\langle \tau_{ij} | u_1^r, u_3^r, \theta^r \rangle$ for small θ^r fluctuations (not shown) is similar to the results for positive θ^r fluctuations. For negative θ^r fluctuations, the levels of anisotropy for different arrays are generally lower, due to the weaker buoyancy effect. Among the four arrays, array 1 has the largest Δ/z and the smallest $-z/L$, and consequently has the highest level of anisotropy and the strongest compression effects associated with the returning flow of large convective eddies. We therefore expect that the SGS stress and its production rate for array 1 are the most challenging to predict by SGS models. The results are important for LES with anisotropic grids (refined in the vertical direction), which are often used near the surface to match the flow interior with the surface (e.g. Mason 1994).

3.6. *Alignment between the conditional SGS stress and its production rate*

The geometric alignment between $\langle \tau_{ij}^d | \boldsymbol{u}^r, \theta^r \rangle$ and $\langle P_{ij}^a | \boldsymbol{u}^r, \theta^r \rangle$ can be characterized by the angles between their eigenvectors. The alignment between $\langle \tau_{ij}^d | \boldsymbol{u}^r \rangle$ and $\langle P_{ij}^a | \boldsymbol{u}^r \rangle$ ($P_{ij}^a = P_{ij} - P_{kk}\delta_{ij}/3$) was first studied by Chen & Tong (2006), who found that $\langle \tau_{ij}^d | u_3^r \rangle$ and $\langle P_{ij}^a | u_3^r \rangle$ are well aligned for positive u_3^r with the alignment angles less than 10°, but are less well aligned for negative u_3^r. Here, we further examine the dependence of the alignment on the temperature fluctuations. The definition of the alignment angles are the same way as those in Chen & Tong (2006). The eigenvalues of the conditional SGS stress tensor, $\langle \tau_{ij}^d | \boldsymbol{u}^r, \theta^r \rangle$, are denoted by α_τ, β_τ and γ_τ, ordered such that $\alpha_\tau \geqslant \beta_\tau \geqslant \gamma_\tau$, and the corresponding unit eigenvectors as $\boldsymbol{\alpha}_\tau$, $\boldsymbol{\beta}_\tau$ and $\boldsymbol{\gamma}_\tau$. Similarly, the eigenvalues of the conditional SGS stress production tensor, $\langle P_{ij}^a | \boldsymbol{u}^r, \theta^r \rangle$, are denoted by α_P, β_P and γ_P, ordered such that $\alpha_P \geqslant \beta_P \geqslant \gamma_P$, and the corresponding unit eigenvectors as $\boldsymbol{\alpha}_P$, $\boldsymbol{\beta}_P$ and $\boldsymbol{\gamma}_P$. Three alignment angles, ψ, ϕ and ξ, are defined as $\psi = \cos^{-1}(|\boldsymbol{\gamma}_P \cdot \boldsymbol{\gamma}_\tau|)$ (the angle between $\boldsymbol{\gamma}_P$ and $\boldsymbol{\gamma}_\tau$), $\phi = \cos^{-1}(|\boldsymbol{\beta}_P \cdot \boldsymbol{\beta}_\tau|)$ and $\xi = \cos^{-1}(|\boldsymbol{\alpha}_P \cdot \boldsymbol{\alpha}_\tau|)$.

The alignment angles shown in figure 11 are generally smaller for positive θ^r fluctuations and larger for negative θ^r fluctuations. In addition, $\langle \tau_{ij}^d | \boldsymbol{u}^r, \theta^r \rangle$ and $\langle P_{ij}^a | \boldsymbol{u}^r, \theta^r \rangle$ are generally well aligned for positive u_3^r and are less so for negative u_3^r. The alignment angles weakly depend on u_1^r, similar to the results of Chen & Tong (2006).

The results for the Lumley triangle (figure 9) show that SGS stress is more anisotropic for $u_3^r > 0$; therefore, there is likely a strong tendency to return to isotropy. Consequently, the pressure destruction rate is better predicted by τ_{ij}/t_Δ, hence the better alignment. In addition, the updrafts with higher temperature ($\theta^r > 0$) generally experience stronger shear near ground, thereby having a large SGS stress production rate. The production and pressure destruction are the dominant terms in the SGS stress transport equation, approximately balancing each other; therefore, the SGS stress and its production rate are well aligned. For $u_3^r < 0$, the Lumley triangle shows that the SGS stress is less anisotropic; therefore, the tendency to return to isotropy may be weak, resulting in poor alignment. Another possible explanation for the poor alignment is that the production rate is small and is no longer a dominant term to balance the pressure destruction rate. It is, however, not clear which term in the SGS stress transport equation causes the imbalance, although Chen & Tong (2006) showed that the vertical advection term is not the cause.

3.7. *SGS model predictions*

The results discussed in the previous parts of this section provide a basis for studying the effects of SGS models on LES statistics. Here we examine the model predictions

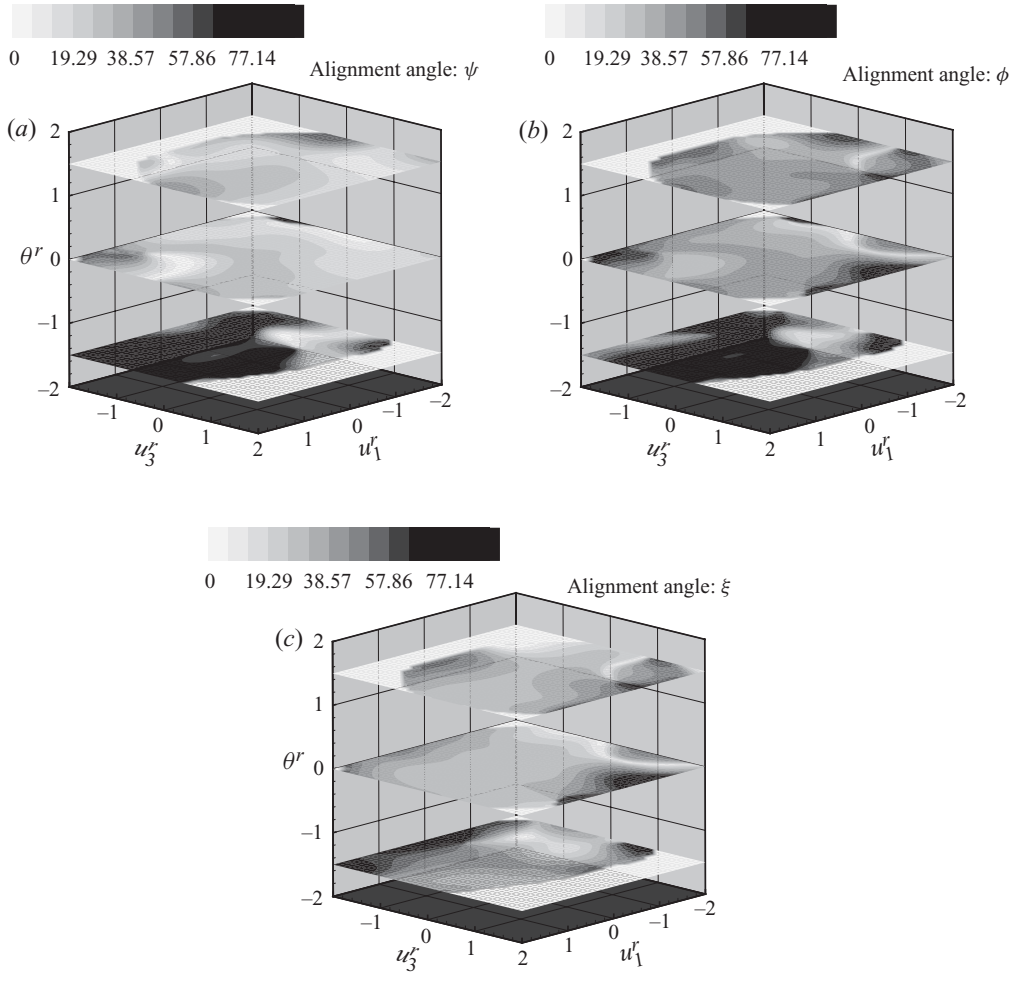

FIGURE 11. Geometric alignment between the conditional SGS stress and its production rate. The alignment angles are small for positive θ^r and increase for negative θ^r and u_3^r.

of $\langle F_i|\boldsymbol{u}^r, \theta^r\rangle$, $\langle P_{F_i}|\boldsymbol{u}^r, \theta^r\rangle$ and $\langle P_\theta|\boldsymbol{u}^r, \theta^r\rangle$ using the Smagorinsky model (Smagorinsky 1963; Lilly 1967), the nonlinear model (Leonard 1974; Clark *et al.* 1979) and the mixed model (Clark *et al.* 1979; Liu *et al.* 1994) by comparing them with the experimental results. We focus on the predictions of the SGS flux and only discuss some of the results for the SGS stress. The mean values of the modelled mean SGS temperature flux components are given in table 5.

In order to compute the modelled SGS temperature flux production rate P_{F_i}, the modelled SGS stress is needed. In this work, the modelled SGS stress is computed using the same procedure as given in Chen & Tong (2006). That study showed that the conditional SGS normal components are underpredicted severely by the Smagorinsky model and are overpredicted slightly by the nonlinear model. The trends of the shear components are generally predicted well by the Smagorinsky model and are poorly predicted by the nonlinear model. The magnitudes of the shear components are generally underpredicted by a factor of two using the Smagorinsky model. The mixed model can predict normal components well but not the shear component. These

results are important for understanding the trends and magnitudes of the conditional SGS temperature flux production rate discussed in the following.

3.7.1. *The Smagorinsky model*

The Smagorinsky model is given by Smagorinsky (1963) and Lilly (1967):

$$F_i^{smg} = -Pr_T^{-1}(C_S\Delta)^2(2S_{mn}S_{mn})^{1/2}\frac{\partial\theta^r}{\partial x_i} \tag{3.6}$$

where $C_s = 0.154$, Pr_T and S_{ij} are the Smagorinsky coefficient for a box filter, the SGS turbulent Prandtl number and the resolvable-scale velocity strain rate, respectively. In this work, we determine $C_s = 0.109$ and $Pr_T^{-1}C_s^2 = 0.0237$ ($Pr_T = 0.50$) by matching the modelled and measured mean SGS energy and temperature variance production rates, respectively. The values are similar to the values obtained by Kleissl *et al.* (2003) and Porté-Agel (2004). The Pr_T value is smaller than the value of 0.7 used by Mason & Brown (1994), probably because the simulation does not attempt to match the mean SGS scalar variance production rate.

Tables 4 and 5 show that the mean horizontal SGS temperature flux is underpredicted severely and the mean vertical SGS temperature flux is underpredicted by approximately 30 %. The predicted conditional means using the Smagorinsky model are shown in figures 12 and 13. Figures 12(*a*) and 2(*a*) show that the horizontal SGS temperature flux, $\langle F_1|\boldsymbol{u}^r, \theta^r\rangle$, is underpredicted, because the model uses only the horizontal temperature gradient $\partial\theta^r/\partial x_1$, which is very small. In addition, the sign of $\langle F_1|\boldsymbol{u}^r, \theta^r\rangle$ for some resolvable-scale velocity and temperature is predicted incorrectly. As discussed in § 3.1, the conditional production of F_1 is dominated by $\langle F_3(\partial u_1^r/\partial x_3)|\boldsymbol{u}^r, \theta^r\rangle$ and $\langle \tau_{13}(\partial\theta^r/\partial x_3)|\boldsymbol{u}^r, \theta^r\rangle$. Because these gradients do not appear in the model, the model cannot account for the dominant production mechanisms, and consequently cannot predict the flux correctly. The results demonstrate the importance of including the effects of the dominant vertical gradient in the modelling of $\langle F_1|\boldsymbol{u}^r, \theta^r\rangle$.

Figures 12(*b*) and 2(*c*) show that the magnitude of the vertical SGS temperature flux, $\langle F_3|\boldsymbol{u}^r, \theta^r\rangle$, is predicted better than that of $\langle F_1|\boldsymbol{u}^r, \theta^r\rangle$, because $\langle F_3^{smg}|\boldsymbol{u}^r, \theta^r\rangle$ uses $\partial\theta^r/\partial x_3$, which is in the dominant term in P_{F_3}. The trend of $\langle F_3|\boldsymbol{u}^r, \theta^r\rangle$ is generally predicted well for positive θ^r fluctuations. The trend for small and negative θ^r fluctuations is not predicted as well.

The trend of the conditional SGS shear stress component $\langle \tau_{13}|\boldsymbol{u}^r, \theta^r\rangle$ for positive θ^r fluctuations (figure 12*c*) is similar to that of $\langle \tau_{13}|\boldsymbol{u}^r\rangle$ and is predicted quite well (figure 8*a*). However, for small and negative θ^r fluctuations it is predicted less well. The magnitude is underpredicted by more than a factor of two. The predictions of the other conditional SGS stress components as well as the conditional SGS stress production rate (not shown) for positive θ^r fluctuations are similar to those without conditioning on θ^r and generally are more accurate than those for negative θ^r fluctuations. The incorrect predictions of the dependencies on θ^r will result in an incorrect conditional velocity in LES, consequently an incorrect resolvable-scale temperature PDF.

The trend of $\langle P_{F_1}|\boldsymbol{u}^r, \theta^r\rangle$ is generally well predicted (figures 13*a* and 3*a*). Because $\langle P_{F1}^{smg}|\boldsymbol{u}^r, \theta^r\rangle$ $(= -\langle \tau_{1k}^{smg}(\partial\theta^r/\partial x_k) + F_k^{smg}(\partial u_1^r/\partial x_k)|\boldsymbol{u}^r, \theta^r\rangle)$ is dominated by $-\langle F_3^{smg}(\partial u_1^r/\partial x_3) + \tau_{13}^{smg}(\partial\theta^r/\partial x_3)|\boldsymbol{u}^r, \theta^r\rangle$, the well-predicted trend of $\langle P_{F_1}|\boldsymbol{u}^r, \theta^r\rangle$ is largely due to the well-predicted trends of τ_{13} and F_3. Its magnitude, however, is underpredicted approximately by a factor of two due to the underpredictions of the magnitudes of τ_{13} (Chen & Tong 2006) and F_3. The trend and magnitude of $\langle P_{F_3}|\boldsymbol{u}^r, \theta^r\rangle$

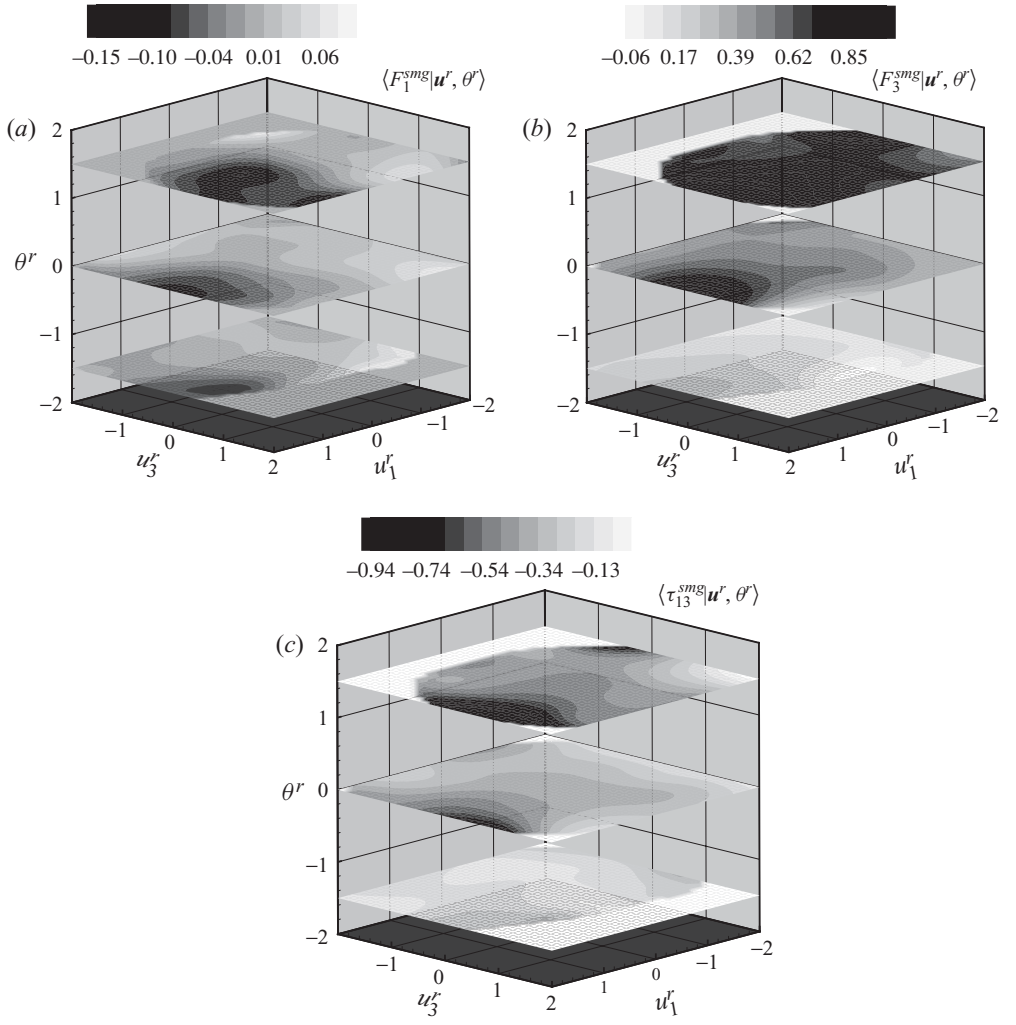

FIGURE 12. Predicted conditional SGS temperature flux and SGS shear stress using the Smagorinsky model. The trends of $\langle F_3|\boldsymbol{u}^r, \theta^r\rangle$ and $\langle \tau_{13}|\boldsymbol{u}^r, \theta^r\rangle$ are well predicted.

are poorly predicted (figures 13*b* and 3*c*). As discussed in § 3.1, $\langle P_{F3}^{smg}|\boldsymbol{u}^r, \theta^r\rangle$ $(= -\langle \tau_{3k}^{smg}(\partial\theta^r/\partial x_k) + F_k^{smg}(\partial u_3^r/\partial x_k)|\boldsymbol{u}^r, \theta^r\rangle)$ is dominated by $\langle -\tau_{33}^{smg}(\partial\theta^r/\partial x_3)|\boldsymbol{u}^r, \theta^r\rangle$. The poor prediction of $\langle P_{F_3}|\boldsymbol{u}^r, \theta^r\rangle$, therefore, is due to the poor prediction of τ_{33} by the Smagorinsky model (Chen & Tong 2006). The trend and magnitude of $\langle P_\theta|\boldsymbol{u}^r, \theta^r\rangle$ generally are predicted well (figures 13*c* and 4), which is likely to lead to well-predicted skewness of θ^r. The dominant term of $\langle P_\theta^{smg}|\boldsymbol{u}^r, \theta^r\rangle$ is $\langle F_3^{smg}(\partial\theta^r/\partial x_3)|\boldsymbol{u}^r, \theta^r\rangle$; therefore, the well-predicted trend (the magnitude is matched) is due to the well-predicted trend of F_3. This result is in contrast with the poor prediction of $\langle P_{33}|{u_3}^r\rangle$. It further suggests that the driving buoyancy force for the positive vertical velocity skewness likely is well predicted; therefore, the underprediction of the skewness is due to the underprediction of $\langle P_{33}|{u_3}^r\rangle$.

The results for the SGS production rates show that when the conditional means of the dominant SGS stress and/or flux components that appear in an SGS production rate are well predicted by an SGS model, the conditional mean of the SGS production

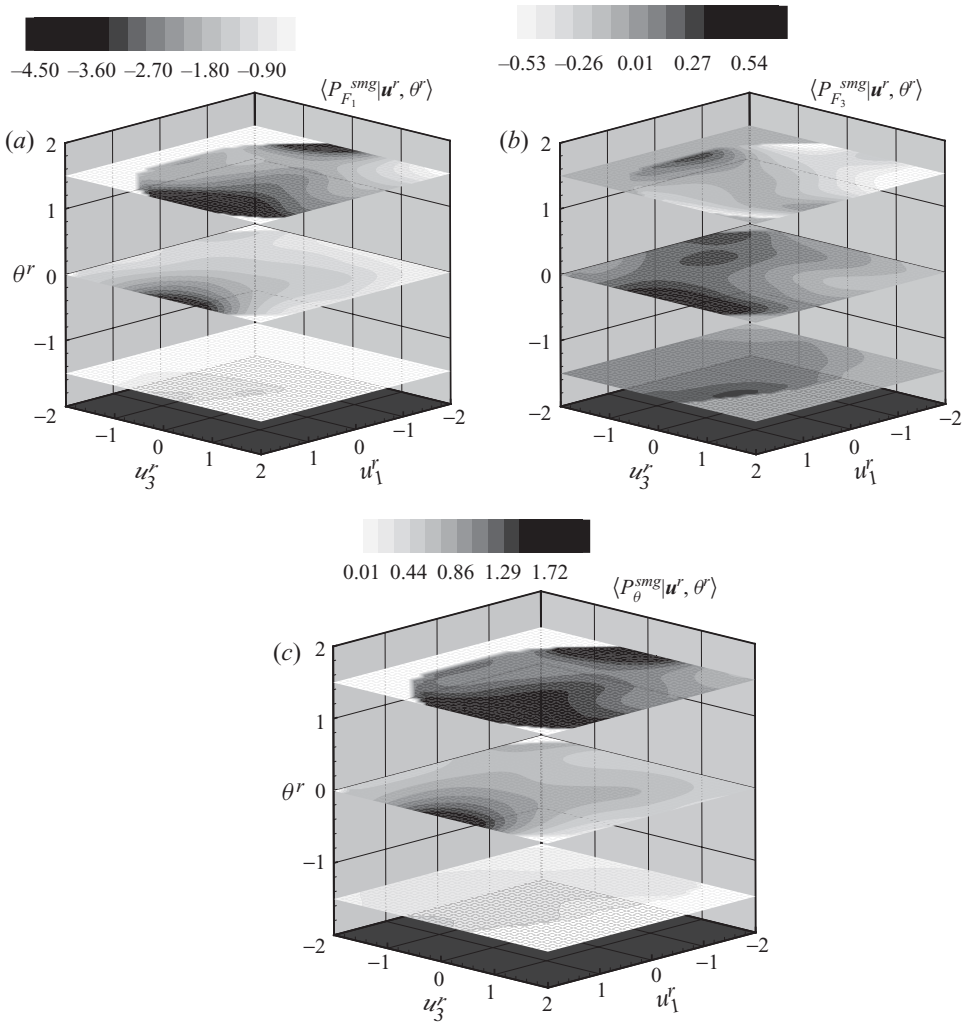

FIGURE 13. Predicted conditional SGS temperature flux production rate and SGS temperature variance production rate using the Smagorinsky model. The trend of $\langle P_{F_1}|\boldsymbol{u}^r, \theta^r\rangle$ is well predicted.

rate is also well predicted. These results suggest that correct predictions of the conditional means are more important than the correlations between the conditional fluctuations of the SGS stress (flux) and the resolvable-scale gradients.

3.7.2. *The nonlinear model*

The nonlinear model (Leonard 1974; Clark *et al.* 1979) is essentially the first-order approximation of the similarity model (Bardina *et al.* 1980) and is given by

$$F_i^{nl} = \frac{1}{12}\Delta^2 \frac{\partial \theta^r}{\partial x_k}\frac{\partial u_i^r}{\partial x_k}. \tag{3.7}$$

Although in the data analysis the velocity and temperature in (3.7) are filtered explicitly in the two horizontal directions, they are effectively three-dimensionally filtered in the terms containing the vertical derivatives, because these derivatives are

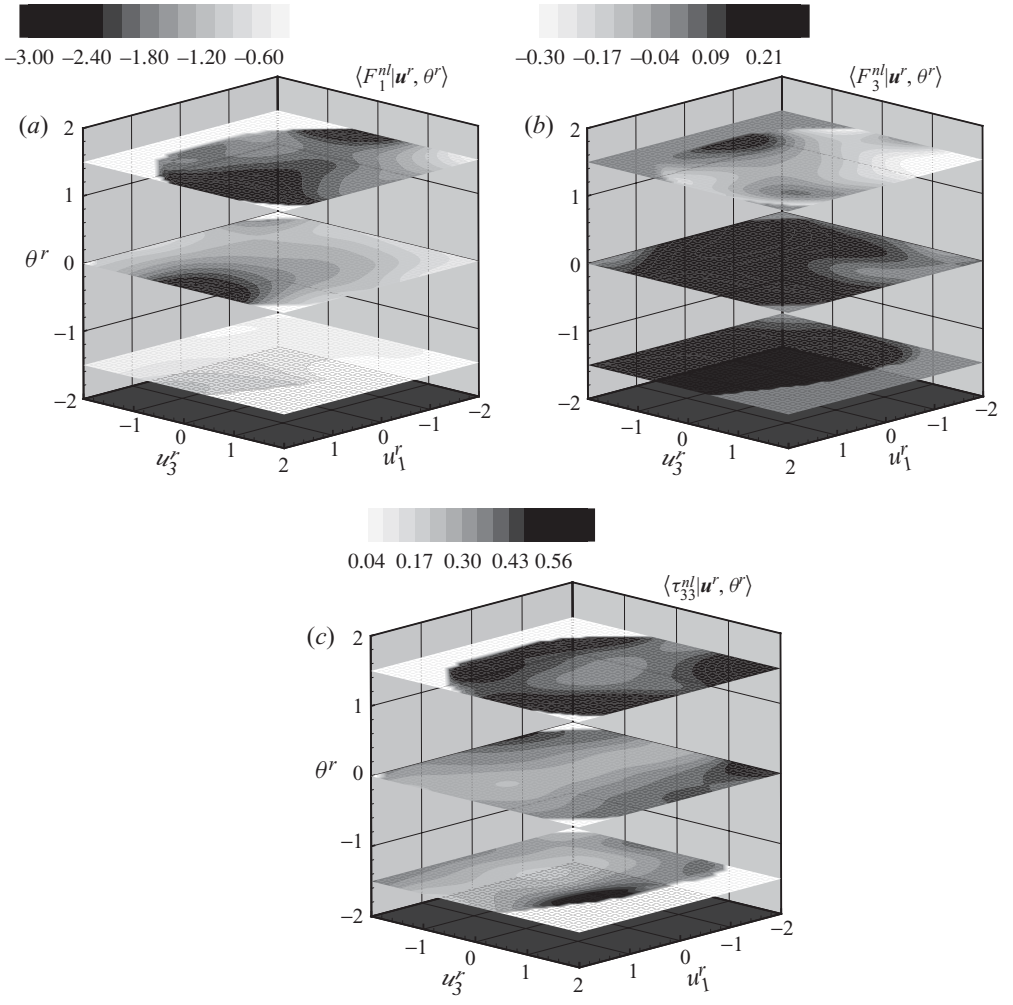

FIGURE 14. Predicted conditional SGS temperature flux and SGS normal stress using the nonlinear model. The trend of $\langle F_1|\boldsymbol{u}^r, \theta^r\rangle$ is well predicted.

obtained using a two-point finite-difference scheme, which is a top-hat filter for the derivatives. The resulting filtered derivatives are equivalent to the derivatives of the filtered variables in (3.7). Inclusion of the terms containing the vertical derivatives, therefore, is consistent with the expansion procedure to obtain the nonlinear model and the definition of the model. It is also consistent with LES using spectral derivatives. The predictions of the nonlinear model are shown in figures 14 and 15. In general, the nonlinear model predicts the overall trend and the magnitude better than the Smagorinsky model. The trend for small θ^r fluctuations is underpredicted but the magnitude is slightly overpredicted.

The mean horizontal SGS temperature flux is overpredicted by approximately 35 % and the mean vertical SGS temperature flux is underpredicted by approximately 80 % (tables 4 and 5). The predicted magnitude of $\langle F_1|\boldsymbol{u}^r, \theta^r\rangle$ (figure 14*a*) using the nonlinear model is better than that of the Smagorinsky model, which can be understood as the following. Our results (not shown) indicate that the model

component $F_1^{nl} = (\partial\theta^r/\partial x_k)(\partial u_1^r/\partial x_k)$ is dominated by $(\partial\theta^r/\partial x_3)(\partial u_1^r/\partial x_3)$, which can be rewritten in Smagorinsky-like terms as

$$F_1^{nl} \sim \frac{\partial\theta^r}{\partial x_3}\frac{\partial u_1^r}{\partial x_3} \propto F_3^{smg}\frac{\partial u_1^r}{\partial x_3} + \tau_{13}^{smg}\frac{\partial\theta^r}{\partial x_3}. \tag{3.8}$$

The results in the previous section show that the trends of τ_{13} and F_3 are predicted well by the Smagorinsky model; therefore, the term $F_3^{smg}(\partial u_1^r/\partial x_3) + \tau_{13}^{smg}(\partial\theta^r/\partial x_3)$ in (3.7) is effectively the Smagorinsky model prediction of $\langle P_{F_1}|\boldsymbol{u}^r, \theta^r\rangle$. Figures 2(*a*), 3(*a*) and 5(*a*) show that the conditional SGS flux and the conditional flux production rate have similar trends, which is likely a result of the balance between the SGS flux production rate and the pressure destruction rate and the fact that the latter can be predicted quite well by the SGS flux and an SGS time scale. Hence, $\langle F_1|\boldsymbol{u}^r, \theta^r\rangle$ is better predicted by the nonlinear model.

The trend of $\langle F_3|\boldsymbol{u}^r, \theta^r\rangle$ is underpredicted (figures 14*b* and 2*c*). Furthermore, $\langle F_3^{nl}|\boldsymbol{u}^r, \theta^r\rangle$ has some spurious negative values. The dominant component of F_3^{nl} is $(\partial\theta^r/\partial x_3)(\partial u_3^r/\partial x_3)$, which can be rewritten as

$$F_3^{nl} \sim \frac{\partial\theta^r}{\partial x_3}\frac{\partial u_3^r}{\partial x_3} \propto \tau_{33}^{smg}\frac{\partial\theta^r}{\partial x_3}. \tag{3.9}$$

Because τ_{33} is poorly predicted by the Smagorinsky model, $(\partial\theta^r/\partial x_3)(\partial u_3^r/\partial x_3)$ is not a good model for the dominant term of P_{F_3}; therefore, $\langle F_3|\boldsymbol{u}^r, \theta^r\rangle$ is poorly predicted by the nonlinear model.

The above analyses relate the performance of the nonlinear model to the Smagorinsky model predictions and the surface layer SGS dynamics. Here we also provide similar analyses of the nonlinear SGS stress model. The normal component of the nonlinear model τ_{11}^{nl} (not shown) for positive θ^r fluctuations is predicted quite well, which can be rewritten as

$$\tau_{11}^{nl} \sim \frac{\partial u_1^r}{\partial x_1}\frac{\partial u_1^r}{\partial x_1} + \frac{\partial u_1^r}{\partial x_2}\frac{\partial u_1^r}{\partial x_2} + \frac{\partial u_1^r}{\partial x_3}\frac{\partial u_1^r}{\partial x_3} \propto \tau_{11}^{smg}\frac{\partial u_1^r}{\partial x_1} + \tau_{12}^{smg}\frac{\partial u_1^r}{\partial x_2} + \tau_{13}^{smg}\frac{\partial u_1^r}{\partial x_3}.$$

Because the trend of τ_{13} is predicted well by the Smagorinsky model, $\tau_{13}^{smg}(\partial u_1^r/\partial x_3)$ is a good model for the dominant term in P_{11}; therefore, τ_{11} is predicted well by the nonlinear model. Similarly, the dominant term in τ_{33}^{nl} (figure 14*c*), $(\partial u_3^r/\partial x_3)(\partial u_3^r/\partial x_3)$, can be written as $\tau_{33}^{smg}(\partial u_3^r/\partial x_3)$. Because τ_{33} is predicted poorly by the Smagorinsky model, so is τ_{33} by the nonlinear model. The predictions of the other conditional SGS stress components as well as the conditional SGS stress production rate (not shown) for positive θ^r fluctuations are similar to those without conditioning on θ^r and are generally more accurate than those for negative θ^r fluctuations.

These model predictions are important for understanding the model prediction of the conditional SGS flux production rate. The magnitude and trend of $\langle P_{F_1}|\boldsymbol{u}^r, \theta^r\rangle$ for positive θ^r fluctuations are not predicted well (figures 15*a* and 3*a*), due to the poor predictions of F_3 and τ_{13}, which are in the dominant terms in $\langle P_{F_1}|\boldsymbol{u}^r, \theta^r\rangle$ $(-\langle F_3(\partial u_1^r/\partial x_3) + \tau_{13}(\partial\theta^r/\partial x_3)|\boldsymbol{u}^r, \theta^r\rangle)$. The magnitude of $\langle P_{F_3}|\boldsymbol{u}^r, \theta^r\rangle$ is underpredicted (figures 15*b* and 3*c*), while the trend for positive θ^r fluctuations is predicted better than that for small and negative θ^r fluctuations, due to the well-predicted trend of τ_{33}, which is in the dominant term of $\langle P_{F_3}|\boldsymbol{u}^r, \theta^r\rangle$ $(\langle -\tau_{33}(\partial\theta^r/\partial x_3)|\boldsymbol{u}^r, \theta^r\rangle)$. Both the trend and magnitude of $\langle P_\theta|\boldsymbol{u}^r, \theta^r\rangle$ (figures 15*c* and 4) are not predicted as well as the Smagorinsky model, due to the poor prediction of F_3, which is in the dominant term of $\langle P_\theta|\boldsymbol{u}^r, \theta^r\rangle$ $(\langle F_3(\partial\theta^r/\partial x_3)|\boldsymbol{u}^r, \theta^r\rangle)$.

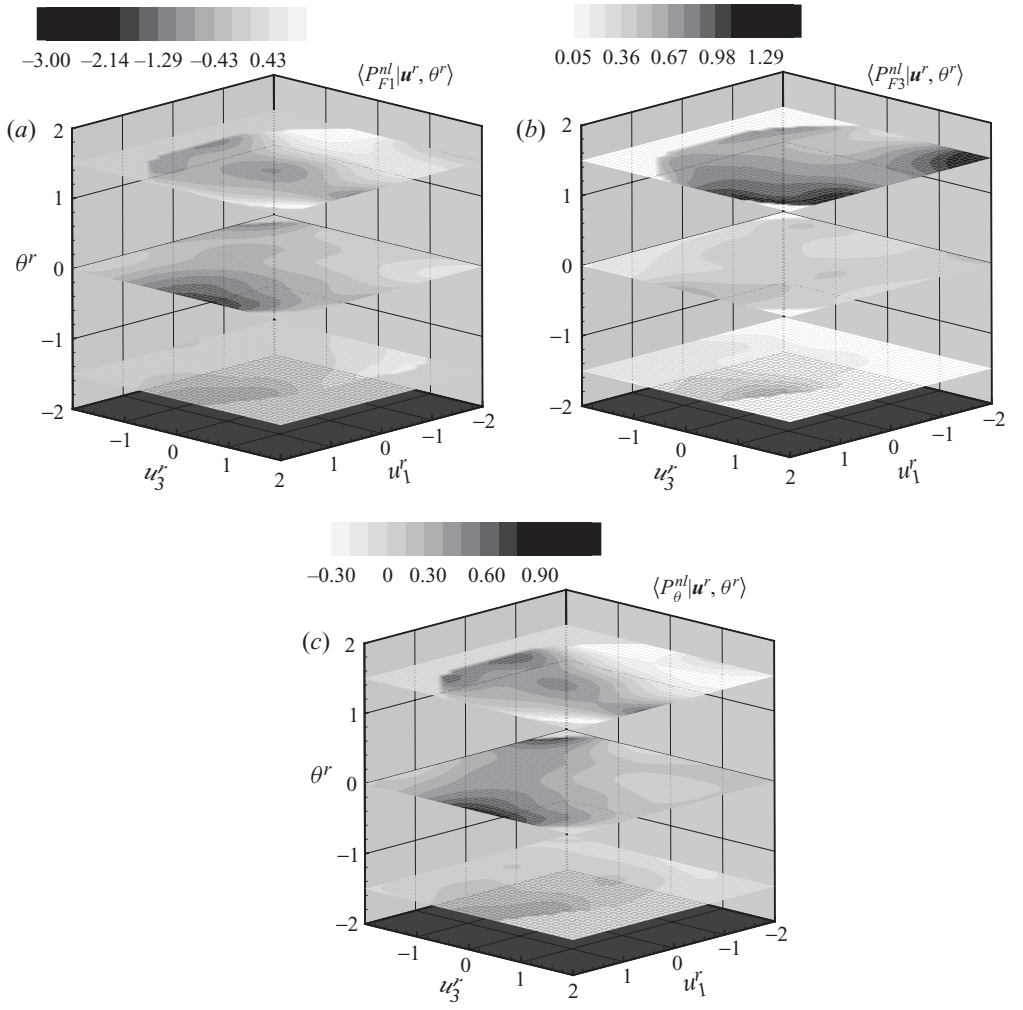

FIGURE 15. Predicted conditional SGS temperature flux production rate and the temperature variance production rate using the nonlinear model.

We note that previous studies (e.g. Vreman, Geurts & Kuerten 1996) have shown that the nonlinear model can result in unstable LES. In this case no *a posteriori* tests of the model under normal flow conditions as well as comparisons with *a priori* tests are possible. Nevertheless, the *a priori* model performance in predicting the other components of the SGS stress production rate and the SGS flux production rate still provides valuable information for understanding models that are based on the nonlinear model (but with much improved predictions of the SGS energy production rate), such as the mixed model, which we examine next.

3.7.3. *The mixed model*

The results discussed above show that the Smagorinsky model can predict quite well $\langle F_3|\boldsymbol{u}^r, \theta^r\rangle$ but not $\langle F_1|\boldsymbol{u}^r, \theta^r\rangle$, and the nonlinear model can predict quite well $\langle F_1|\boldsymbol{u}^r, \theta^r\rangle$ but not $\langle F_3|\boldsymbol{u}^r, \theta^r\rangle$. A mixed model combining these two models, as done

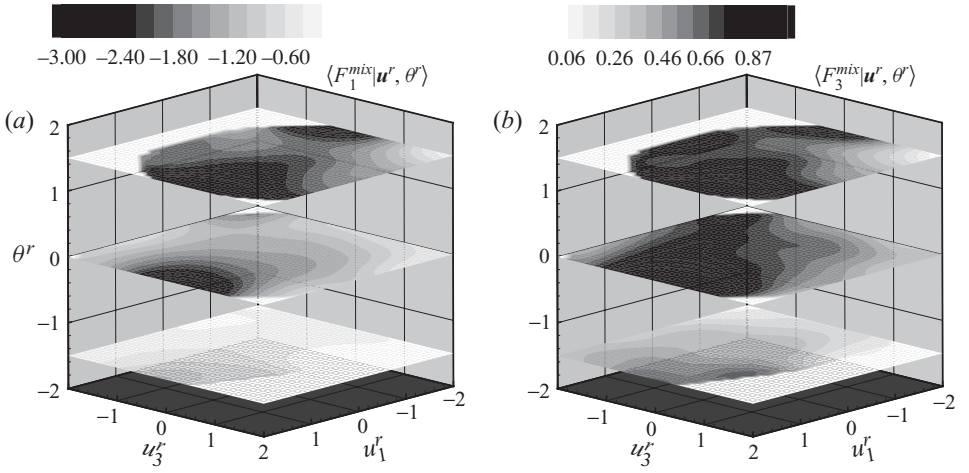

FIGURE 16. Predicted conditional SGS temperature flux using the mixed model.

for SGS stress (Clark *et al.* 1979; Liu *et al.* 1994),

$$F_i^{mix} = \frac{1}{12}\Delta^2 \frac{\partial \theta^r}{\partial x_k}\frac{\partial u_i^r}{\partial x_k} - Pr_T^{-1}(C_S\Delta)^2(2S_{mn}S_{mn})^{1/2}\frac{\partial \theta^r}{\partial x_i}, \tag{3.10}$$

therefore, can potentially provide improved predictions.

Table 5 shows that the mean horizontal SGS temperature flux is overpredicted by approximately 35 % and the mean vertical SGS temperature flux is underpredicted by approximately 25 %. The conditional SGS statistics predicted by the mixed model are shown in figures 16 and 17. The predicted magnitude and trend of $\langle F_1|\boldsymbol{u}^r,\theta^r\rangle$ (figure 16*a*) are close to the predictions of the nonlinear model (figure 14*a*), due to the underpredicted magnitude of $\langle F_1|\boldsymbol{u}^r,\theta^r\rangle$ by the Smagorinsky part of the model. The predicted trend of $\langle F_3|\boldsymbol{u}^r,\theta^r\rangle$ (figure 16*b*) is between the predictions of the Smagorinsky model (figure 12*b*) and the nonlinear model (figure 14*b*), because the magnitude of $\langle F_3^{nl}|\boldsymbol{u}^r,\theta^r\rangle$ is comparable to that of $\langle F_3^{smg}|\boldsymbol{u}^r,\theta^r\rangle$.

The trend of $\langle P_{F1}^{mix}|\boldsymbol{u}^r,\theta^r\rangle$ (figure 17*a*) is close to the prediction of the nonlinear model (figure 15*a*) but the variations of the magnitude are improved, because the mixed model predictions of F_3 and τ_{13} are better than the nonlinear model, (although not as good as the Smagorinsky model). The magnitude of $\langle P_{F3}^{mix}|\boldsymbol{u}^r,\theta^r\rangle$ (figure 17*b*) is close to the prediction of the nonlinear model (figure 15*b*), because the magnitude of $\langle P_{F3}^{smg}|\boldsymbol{u}^r,\theta^r\rangle$ is smaller than that of $\langle P_{F3}^{nl}|\boldsymbol{u}^r,\theta^r\rangle$. The trend of $\langle P_{\theta}^{mix}|\boldsymbol{u}^r,\theta^r\rangle$ (figure 17*c*) is between those of $\langle P_{\theta}^{nl}|\boldsymbol{u}^r,\theta^r\rangle$ (figure 15*c*) and $\langle P_{\theta}^{smg}|\boldsymbol{u}^r,\theta^r\rangle$ (figure 13*c*), i.e. not as good as that of the Smagorinsky model but better than that of the nonlinear model. The mixed model predictions of the conditional SGS stress and the conditional SGS stress production rate are also a compromise between the Smagorinsky model and the nonlinear model.

3.8. *Potential effects of SGS models on the resolvable-scale statistics*

The conditional SGS fluxes and their production rates discussed above govern the evolution of the resolvable-scale velocity–temperature JPDF through (1.6). Deviations of SGS model predictions from their true values will lead to inaccuracies in the predicted JPDF. Chen & Tong (2006) discussed the potential effects of the modelled SGS stress and the SGS stress production rate on the resolvable-scale velocity JPDF.

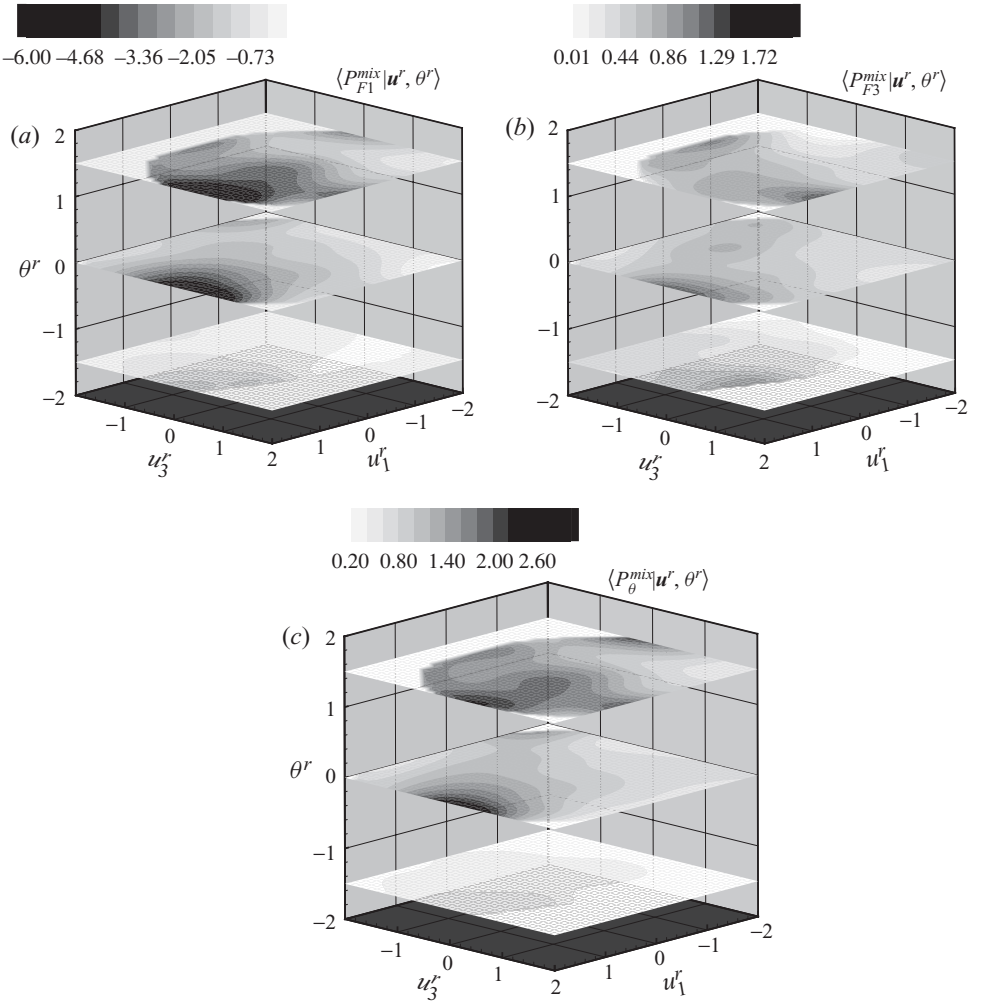

FIGURE 17. Predicted conditional SGS temperature flux production rate and the SGS temperature variance production rate using the mixed model.

Here, we focus on the potential effects of SGS model predictions on the velocity–temperature JPDF.

The results of this paper show that the conditional horizontal temperature flux production rate is dominated by $\langle -F_3(\partial u_1^r/\partial x_3)|\boldsymbol{u}^r, \theta^r\rangle$ and $\langle -\tau_{13}(\partial\theta^r/\partial x_3)|\boldsymbol{u}^r, \theta^r\rangle$, while the conditional vertical temperature flux production rate is dominated by $\langle -\tau_{33}(\partial\theta^r/\partial x_3)|\boldsymbol{u}^r, \theta^r\rangle$. Correct predictions of F_3, τ_{13} and τ_{33}, therefore, are critical for reproducing the resolvable-scale velocity–temperature JPDF. Note that τ_{13} and τ_{33} affect the resolvable-scale temperature and velocity–temperature joint statistics not only through their influence on the resolvable-scale velocity, but also more directly through the SGS flux production rate.

The Smagorinsky model underpredicts the conditional horizontal SGS temperature flux, but predicts well the trend of the conditional vertical SGS temperature flux. Although the underprediction of the conditional horizontal SGS temperature flux in a horizontally homogeneous ABL has no consequences, in other types of flows, such

as a surface layer above sloped terrain, it will directly affect the temperature PDF and the velocity–temperature JPDF. The model also underpredicts $\langle \tau_{33} | \boldsymbol{u}^r, \theta^r \rangle$ (Chen & Tong 2006). Because τ_{33} appears in the dominant term of the conditional vertical temperature flux production rate, $\tau_{33}(\partial\theta^r/\partial x_3)$, the underprediction of $\langle \tau_{33} | \boldsymbol{u}^r, \theta^r \rangle$ causes an underprediction of the conditional vertical temperature flux production rate, which in turn will result in an underprediction of the resolvable-scale vertical temperature flux (velocity–temperature correlation). Consequently, the total vertical flux is underpredicted. With a constant heat flux boundary condition, the mean temperature gradient will be overpredicted, because the LES fields have to self-adjust to carry the correct magnitude of heat flux at the surface. The improved mean temperature profile using the split model (Sullivan *et al.* 1994) and the stochastic model (Mason & Thomson 1992) may be partly because these models provide improved predictions of τ_{13} and τ_{33}, which are important for predicting the temperature flux production rate.

The dynamic Smagorinsky model and its variants (e.g. Porté-Agel 2004) can provide different predictions of the mean temperature gradient than the Smagorinsky model. Nonetheless, in these models the assumption of proportionality between the SGS temperature flux and the resolvable-scale temperature gradient still remains. As a result, the temperature variance transfer rate from the resolvable to the subgrid scales is likely to be predicted incorrectly. In addition, the role played by τ_{33} cannot be accounted for by changing the model coefficient in the dynamic Smagorinsky model. Consequently, while there may exist a value of the model coefficient that will produce the correct mean temperature gradient, the models are unlikely to predict correctly other resolvable-scale statistics.

The nonlinear model can predict quite well the conditional horizontal SGS temperature flux but not the vertical SGS flux. Again, due to the constant heat flux boundary condition, the underprediction of the vertical SGS temperature flux will cause an overprediction of the mean temperature gradient. The underpredictions of the conditional F_3 and τ_{13} also cause an underprediction of the conditional P_{F_1}, which will result in an underprediction of the horizontal resolvable-scale temperature flux.

These potential SGS model effects indicate that for LES to reproduce a resolvable-scale statistic, all the relevant conditional SGS stress, flux and SGS production rates must be correctly predicted. An example of violation of this condition is the poor prediction of $\langle \tau_{33} | \boldsymbol{u}^r, \theta^r \rangle$ by the Smagorinsky model, which can lead to an incorrect prediction of the conditional P_{F_3}, and hence the resolvable-scale vertical temperature flux, even when F_3 is quite well predicted. Previous efforts to improve SGS models generally have focused on the model predictions of the SGS stress and flux. The results in the present study show that in addition to the SGS stress and flux, the predictions of the SGS production rates must also be improved.

We note that although a velocity field is not affected by a passive scalar advected by the velocity, velocity statistics conditional on the scalar, such as the conditional SGS stress and the conditional SGS stress production rate, are generally dependent on the scalar. The dependencies are partly a result of the different flow histories that the SGS eddies with the same resolvable-scale velocity but different resolvable-scale scalar values have experienced (Chen *et al.* 2005). Incorrect predictions of the dependencies will result in an incorrect conditional velocity, $\langle \boldsymbol{u} | \theta \rangle$, and consequently in an incorrect resolvable-scale temperature PDF.

The statistical SGS model test approach in the present study is based on the necessary conditions given by the resolvable-scale velocity–scalar joint JPDF equation.

Thus, we expect some differences between the *a priori* and *a posteriori* SGS model performance. The results in Chen *et al.* (2009), however, show remarkable consistency between the two types of tests. Their model tests also show that the differences between the *a priori* and *a posteriori* model predictions of the conditional SGS stress and the conditional SGS stress production rate are generally smaller than the differences between the modelled (*a priori* or *a posteriori*) and the true values of these statistics. This suggests that the deviations of the model predictions from the measurements are primarily a result of the characteristics (deficiencies) of the model, whereas the (relatively smaller) differences of the two types of test results are due to the different model inputs (measured turbulence fields and LES fields). In view of the JPDF equation, the similarity between the *a priori* and *a posteriori* test results suggests that both are consistent with the JPDF obtained in LES. Under such conditions, the *a priori* model performance is consistent with the *a posteriori* performance.

When an SGS model (e.g. the nonlinear model) results in unstable LES, a comparison between *a priori* and *a posteriori* tests is not possible. The question of consistency between the two types of tests becomes whether the *a priori* tests can predict the divergence of the moments of the JPDF (equivalent to unstable LES) using the JPDF equation. The severe underprediction of the SGS energy production rate by the nonlinear model (by a factor of two) is consistent with the divergence of the kinetic energy in LES. A physical example of such an energy transfer rate imbalance is a homogeneous shear flow, in which the turbulent kinetic energy dissipation rate is approximately 60 % of the production, causing the energy to increase exponentially in time. This observation suggests that it may be possible to predict divergence of the moments of the JPDF using *a priori* results. Further investigations of the JPDF equation are needed to answer this question.

4. Conclusions

In this study, we used the field measurement data in a convective atmospheric boundary layer to analyse the SGS statistics that evolve the resolvable-scale velocity–temperature JPDF. These statistics must be predicted correctly by SGS models for LES to reproduce the JPDF. The results show that the statistics, including the conditional SGS temperature flux, its production rate and the SGS temperature variance production rate conditional on the resolvable-scale velocity and temperature, depend strongly on the resolvable-scale velocity and temperature, and the dependencies are closely related to the surface layer dynamics. SGS model predictions of these SGS statistics, therefore, have strong effects on LES statistics.

The analyses show that for the stability conditions studied, the dependencies are generally strong for positive resolvable-scale temperature fluctuations and are weak for negative fluctuations. For positive θ^r fluctuations, eddies associated with updrafts, which generally come from the near-ground region and experience strong shear and vertical temperature gradient, contain large amounts of vertical SGS flux and SGS stress, resulting in large SGS flux production rates. For small θ^r fluctuations, eddies are generally well mixed; therefore, the results tend to be more symmetric with respect to the vertical velocity, u_3^r. For negative θ^r fluctuations, eddies associated with downdrafts, which generally come from the mixed layer region, carry relatively small fluxes, resulting in a weak dependence of the conditional SGS temperature flux production rate on the resolvable-scale velocity. The model predictions for positive θ^r fluctuations, therefore, may have a stronger impact on LES statistics.

The conditional SGS temperature flux and the conditional SGS temperature flux production rate have similar trends and are generally aligned well for positive θ^r fluctuations with the alignment angle being generally less than 10°, consistent with the balance between the production rate and the pressure destruction rate and the use of the ratio of the SGS temperature flux to a time scale as a model for the pressure destruction rate. The similarities and the dynamic connections between the conditional temperature flux and its production rate suggest the potential of using the conditional temperature flux production rate to model the temperature flux in convective ABLs. For example, assuming that the boundary layer is in local equilibrium, the balance between the SGS flux production rate and the pressure destruction combined with a model using the ratio of the SGS flux to the time scale can provide a model for the SGS flux.

The Lumley triangle representation of the conditional SGS stress shows that the anisotropy of $\langle \tau_{ij} | u_1^r, u_3^r, \theta^r \rangle$ for positive θ^r fluctuations is strong and is close to the that of $\langle \tau_{ij} | u_1^r, u_3^r \rangle$ (without conditioning on θ^r). The conditional SGS stress is not far from being axisymmetric with either one small or one large eigenvalue. For small θ^r fluctuations, the results are somewhat similar to the results for positive θ^r fluctuations. For negative θ^r fluctuations, the conditional SGS stress is less anisotropic. The conditional SGS stress and its production are generally aligned well for positive θ^r fluctuations but are much less so for negative θ^r, consistent with the results on the Lumley triangle and the possible quasi-equilibrium between the SGS stress production and pressure destruction.

We argue that the dependencies of the SGS stress and its production rate on the resolvable-scale temperature fluctuations are partly due to flow history effects. Incorrect SGS model predictions of these dependencies will result in an incorrect temperature PDF. In addition, modelling of the dependencies to account for flow-history effects might also be beneficial to the prediction of velocity fields.

Our statistical *a priori* tests using these conditional statistics show that the Smagorinsky model underpredicts the conditional horizontal temperature flux but predicts quite well the conditional vertical SGS temperature flux, because it uses the dominant vertical temperature gradients. The model also predicts quite well the trend of the conditional horizontal temperature flux production rate, because the conditional means of τ_{13} and F_3 are quite well predicted. It, however, poorly predicts the conditional vertical SGS temperature flux production rate due to its poor prediction of τ_{33}. The trend of the conditional temperature variance production rate is well predicted because the trend of F_3 is predicted well, which may lead to a better prediction of the resolvable-scale temperature skewness.

The nonlinear model predicts quite well the conditional horizontal SGS temperature flux, while both the conditional horizontal and vertical SGS temperature flux production rates are underpredicted. The prediction of the SGS flux using the nonlinear model is found to be closely related to the predictions of the Smagorinsky model and the quasi-equilibrium between the production and pressure destruction rates, providing a physical explanation of the performance of the nonlinear model. A similar analysis of the nonlinear SGS stress model is also performed.

These analyses of the SGS models show that the current SGS models have varying levels of performance in predicting different SGS components. Often the poor prediction of one SGS flux component affects the prediction of the production rate of another SGS flux component, thereby resulting in errors in the LES statistics that depend on the production rate. Efforts to improve SGS models, therefore, need to ensure that all the relevant SGS fluxes related to the LES

statistics of interest or of importance to the intended applications are predicted correctly.

The statistical *a priori* tests in Chen & Tong (2006) and in the present work demonstrate the importance of modelling the conditional SGS stress, flux and SGS production rate for LES to reproduce resolvable-scale statistics correctly. As noted in the introduction, these *a priori* tests are qualitatively different from the traditional ones, and have shown a high degree of consistency with our *a posteriori* tests (Chen *et al.* 2009). These and the present studies show that our tests based on the conditional SGS stress, flux and SGS production rate are a highly effective approach for identifying SGS model deficiencies and for evaluating model performance in simulations, at least when the model produces stable LES. These studies also provide impetus to further investigation of the JPDF equation. In particular, analytical results on the dependence of the JPDF on the conditional SGS terms (similar to those obtained by Sinai & Yahkot 1989; Pope & Ching 1993; Jaberi *et al.* 1996; Sabelnikov 1998) will be useful for understanding the model effects on the LES statistics and for improving SGS models.

We thank Drs Tom Horst, Don Lenschow, Chin-Hoh Moeng, Peter Sullivan and Jeff Weil at NCAR for conducting the field campaign of the HATS collaboration and for providing the data. This work was supported by the National Science Foundation through grants ATM-0222421 and ATM-0638392.

REFERENCES

Bardina, J., Ferziger, J. H. & Reynolds, W. C. 1980 Improved subgrid scale models for large eddy simulation. *Paper* 80-1357. AIAA.

Borue, V. & Orszag, S. 1998 Local energy flux and subgrid-scale statistics in three-dimensional turbulence. *J. Fluid Mech.* **366**, 1–31.

Businger, J. A., Wyngaard, J. C., Izumi, Y. & Bradley, E. F. 1971 Flux–profile relationships in the atmospheric surface layer. *J. Atmos. Sci.* **28**, 181–189.

Cerutti, S., Meneveau, C. & Knio, O. M. 2000 Spectral and hyper eddy viscosity in high-Reynolds-number turbulence. *J. Fluid Mech.* **421**, 307–338.

Chen, Q., Otte, M., Sullivan, P. P. & Tong, C. 2009 *A posteriori* subgrid-scale model tests based on the conditional means of subgrid-scale stress and its production rate. *J. Fluid Mech.* **626**, 149–181.

Chen, Q. & Tong, C. 2006 Investigation of the subgrid-scale stress and its production rate in a convective atmospheric boundary layer using measurement data. *J. Fluid Mech.* **547**, 65–104.

Chen, Q., Wang, D., Zhang, H. & Tong, C. 2005 Effects of subgrid-scale turbulence on resolvable-scale velocity–scalar statistics. *J. Turbulence* **6**, 36.

Chen, Q., Zhang, H., Wang, D. & Tong, C. 2003 Subgrid-scale stress and its production rate: conditions for the resolvable-scale velocity probability density function. *J. Turbulence* **4**, 027.

Clark, R. A., Ferziger, J. H. & Reynolds, W. C. 1979 Evaluation of subgrid-models using an accurately simulated turbulent flow. *J. Fluid Mech.* **91**, 1–16.

Domaradzki, J. A., Liu, W. & Brachet, M. E. 1993 An analysis of subgrid-scale interactions in numerically simulated isotropic turbulence. *Phys. Fluids* A **5**, 1747–1759.

Edsall, R. M., Thomson, D. W., Wyngaard, J. C. & Peltier, L. J. 1995 A technique for measurement of resolvable-scale flux budgets. In *11th Symposium on Boundary Layers and Turbulence*, pp. 15–17. American Meteorological Society.

Härtel, C., Kleiser, L., Unger, F. & Friedrich, R. 1994 Subgrid-scale energy-transfer in the near-wall region of turbulent flow. *Phys. Fluids* **6**, 3130–3143.

Higgins, C. W., Meneveau, C. & Parlange, M. B. 2007 The effect of filter dimension on the subgrid-scale stress, heat flux, and tensor alignments in the atmospheric surface layer. *J. Atmos. Ocean. Tech.* **24**, 360–375.

Horst, T. W., Kleissl, J., Lenschow, D. H., Meneveau, C., Moeng, C.-H., Parlange, M. B., Sullivan, P. P. & Weil, J. C. 2004 HATS: field observations to obtain spatially-filtered turbulence fields from transverse arrays of sonic anemometers in the atmospheric surface flux layer. *J. Atmos. Sci.* **61**, 1566–1581.

Jaberi, F. A., Miller, R. S. & Givi, P. 1996 Conditional statistics in turbulent scalar mixing and reaction. *AIChE J.* **42**, 1149–1152.

Juneja, A. & Brasseur, J. G. 1999 Characteristics of subgrid-resolved-scale dynamics in anisotropic turbulence, with application to rough-wall boundary layers. *Phys. Fluids* **11**, 3054–3068.

Kaimal, J. C., Wyngaard, J. C., Izumi, Y. & Coté, O. R. 1972 Spectral characteristic of surface-layer turbulence. *Q.J.R. Met. Soc.* **98**, 563–589.

Kelly, M., Wyngaard, J. C. & Sullivan, P. P. 2009 Application of a subfilter-scale flux model over the ocean using OHATS field data. *J. Atmos. Sci.* **66**, 3217–3225.

Kleissl, J., Meneveau, C. & Parlange, M. 2003 On the magnitude and variability of subgrid-scale eddy-diffusion coefficients in the atmospheric surface layer. *J. Atmos. Sci.* **60**, 2372–2388.

Lenschow, D. H. & Stephens, P. L. 1980 The role of thermals in the convective boundary layer. *Bound. Layer Meteor.* **19**, 509–532.

Leonard, A. 1974 Energy cascade in large-eddy simulations of turbulent fluid flows. *Adv. Geophys.* **18**, 237–248.

Lilly, D. K. 1967 The representation of small-scale turbulence in numerical simulation experiments. In *Proceedings of IBM Scientific Computing Symposium on Environment Science*, p. 195.

Liu, S., Meneveau, C. & Katz, J. 1994 On the properties of similarity subgrid-scale models as deduced from measurements in a turbulent jet. *J. Fluid Mech.* **275**, 83–119.

Lumley, J. L. 1978 Computational modeling of turbulent flows. *Adv. Appl. Mech.* **18**, 123–176.

Lund, T. S. & Novikov, E. A. 1992 Parametrization of subgrid-scale stress by the velocity gradient tensor. In *Annual Research Briefs*, pp. 27–43. Stanford, CA: Center for Turbulence Research.

Mason, P. J. 1994 Large-eddy simulation: a critical review of the technique. *Q. J. Roy. Meteorol. Soc.* **120**, 1–26.

Mason, P. J. & Brown, A. R. 1994 The sensitivity of large-eddy simulations of turbulent shear flows to subgrid-scale models. *Bound.-Layer Meteorol.* **70**, 133–150.

Mason, P. J. & Thomson, D. J. 1992 Stochastic backscatter in large-eddy simulation of boundary layers. *J. Fluid Mech.* **242**, 51–78.

McMillan, O. J. & Ferziger, J. H. 1979 Direct testing of subgrid-scale models. *Am. Inst. Aeronaut. Astronaut. J.* **17**, 1340–1346.

Meneveau, C. 1994 Statistics of turbulence subgrid-scale stress: necessary conditions and experimental tests. *Phys. Fluids* **6**, 815.

Moeng, C.-H. 1984 Large-eddy simulation model for the study of planetary boundary-layer turbulence. *J. Atmos. Sci.* **41**, 2052–2062.

Nieuwstadt, F. T. M. & de Valk, J. P. J. M. M. 1987 A large eddy simulation of buoyant and non-buoyant plume dispersion in the atmospheric boundary layer. *Atmos. Environ.* **21**, 2573–2587.

Peltier, L. J., Wyngaard, J. C., Khanna, S. & Brasseur, J. 1996 Spectra in the unstable surface layer. *J. Atmos. Sci.* **53**, 49–61.

Piomelli, U. 1993 High Reynolds-number calculations using the dynamic subgrid-scale stress model. *Phys. Fluids* A **5**, 1484–1490.

Piomelli, U., Moin, P. & Ferziger, J. H. 1988 Model consistency in large eddy simulation of turbulent channel flows. *Phys. Fluids* **31**, 1884–1891.

Pope, S. B. 1985 PDF methods for turbulent reacting flows. *Prog. Engng Combust. Sci.* **11**, 119–192.

Pope, S. B. 2000 *Turbulent Flows*. Cambridge University Press.

Pope, S. B. & Ching, E. 1993 Stationary probability density function in turbulence. *Phys. Fluids* A **5**, 1529–1531.

Porté-Agel, F. 2004 A scale-dependent dynamic model for scalar flux transport in large-eddy simulation of the atmospheric surface layer. *Bound. Layer Meteorol.* **112**, 81–105.

Porté-Agel, F., Parlange, M. B., Meneveau, C. & Eichinger, W. E. 2001 *A priori* field study of the subgrid-scale heat fluxes and dissipation in the atmospheric surface layer. *J. Atmos. Sci.* **58**, 2673–2698.

Rajagopalan, A. G. & Tong, C. 2003 Experimental investigation of scalar–scalar-dissipation filtered joint density function and its transport equation. *Phys. Fluids* **15**, 227–244.

Sabelnikov, V. A. 1998 Asymptotic solution of the equation for the probability distribution of a passive scalar in grid turbulence with a uniform mean scalar gradient. *Phys. Fluids* **10**, 753–755.

Sarghini, F., Piomelli, U. & Balaras, E. 1999 Scale-similar models for large-eddy simulations. *Phys. Fluids* **11**, 1596–1607.

Sinai, Y. G. & Yahkot, V. 1989 Limiting probability distribution of a passive scalar in a random velocity field. *Phys. Rev. Lett.* **63**, 1962–1964.

Smagorinsky, J. 1963 General circulation experiments with the primitive equations. Part I. The basic equations. *Mon. Weather Rev.* **91**, 99–164.

Sullivan, P. P., Horst, T. W., Lenschow, D. H., Moeng, C.-H. & Weil, J. C. 2003 Structure of subfilter-scale fluxes in the atmospheric surface layer with application to large-eddy simulation modeling. *J. Fluid Mech.* **482**, 101–139.

Sullivan, P. P., McWilliams, J. C. & Moeng, C.-H. 1994 A subgrid-scale model for large-eddy simulation of planetary boundary-layer flows. *Bound. Layer Meteorol.* **71**, 247–276.

Tao, B., Katz, J. & Meneveau, C. 2000 Geometry and scale relationships in high Reynolds number turbulence determined from three-dimensional holographic velocimetry. *Phys. Fluids* **12**, 941–944.

Tong, C. 2001 Measurements of conserved scalar filtered density function in a turbulent jet. *Phys. Fluids* **13**, 2923–2937.

Tong, C., Wyngaard, J. C. & Brasseur, J. G. 1999 Experimental study of subgrid-scale stress in the atmospheric surface layer. *J. Atmos. Sci.* **56**, 2277–2292.

Tong, C., Wyngaard, J. C., Khanna, S. & Brasseur, J. G. 1997 Resolvable- and subgrid-scale measurement in the atmospheric surface layer. In *12th Symposium on Boundary Layers and Turbulence*, pp. 221–222. American Meteorological Society.

Tong, C., Wyngaard, J. C., Khanna, S. & Brasseur, J. G. 1998 Resolvable- and subgrid-scale measurement in the atmospheric surface layer: technique and issues. *J. Atmos. Sci.* **55**, 3114–3126.

Vreman, B., Geurts, B. & Kuerten, H. 1996 Large-eddy simulation of the temporal mixing layer using the Clark model. *Theor. Comput. Fluid Dyn.* **8**, 309–324.

Wand, M. P. & Jones, M. C. 1995 *Kernel Smoothing*. Chapman & Hall/CRC.

Wang, D. & Tong, C. 2002 Conditionally filtered scalar dissipation, scalar diffusion, and velocity in a turbulent jet. *Phys. Fluids* **14**, 2170–2185.

Wang, D., Tong, C. & Pope, S. B. 2004 Experimental study of velocity filtered joint density function and its transport equation. *Phys. Fluids* **16**, 3599–3613.

Wyngaard, J. C. 1988 Structure of the PBL. In *Lectures on Air Pollution Modeling*, p. 385. American Meteorological Society.